Compositional Controls on the Distribution of Brine in Europa's Ice Shell

Natalie S. Wolfenbarger[1], Mark G Fox-Powell[2], Jacob Buffo[3], Krista M. Soderlund[4], and Donald D Blankenship[4]

[1]Institute for Geophysics, John A. and Katherine G. Jackson School of Geosciences, University of Texas at Austin
[2]Open University
[3]Dartmouth College
[4]University of Texas at Austin

November 30, 2022

Abstract

The composition of impurities in ice controls the stability of liquid water and thus the distribution of potential aqueous habitats. We present a framework for modeling the brine volume fraction in impure water ice as a polynomial function of temperature and bulk ice salinity, inspired by models originally developed for sea ice. We applied this framework to examine the distribution of brine within the thermally conductive layer of Europa's ice shell, considering binary (NaCl and MgSO4) and multi-ion "analog" (Cl-dominated and SO4-dominated) endmember impurity compositions. We found the vertical extent of brine in a conductive ice layer, expressed as a fraction of the total layer thickness, to be <12% for NaCl, <2% for MgSO4, and <18% for both the analog endmember impurity compositions, suggesting that the depth where brine is stable in an ice shell is more sensitive to composition when only two ionic species are present. For the same temperature and bulk ice salinity, the brine volume fraction is higher in a Cl-dominated ice shell than a SO4-dominated ice shell. Pressure, governed by the ice thickness, was found to have only a minor effect on the vertical extent of brine within an ice shell, relative to temperature and bulk salinity. The minimum stable bulk ice shell salinity formed through freezing of an ocean was found to be insensitive to composition and ultimately governed by the magnitude of the assumed percolation threshold.

Compositional Controls on the Distribution of Brine in Europa's Ice Shell

N. S. Wolfenbarger[1], M. G. Fox-Powell[2], J. J. Buffo[3], K. M. Soderlund[1], D. D. Blankenship[1]

[1]Institute for Geophysics, Jackson School of Geosciences, University of Texas at Austin, Austin, Texas, USA

[2]AstrobiologyOU, The Open University, Walton Hall, Milton Keynes, UK

[3]Dartmouth College, Hanover, New Hampshire, USA

Key Points:

- The brine volume fraction of impure water ice can be represented as a polynomial function of temperature and bulk ice salinity.
- For the same temperature and bulk salinity, the brine volume fraction in a Cl-dominated ice shell is higher than a SO_4-dominated ice shell.
- The magnitude of the percolation threshold governs the minimum fraction of salt entrained in ice formed through freezing of an ocean.

Corresponding author: Natalie S. Wolfenbarger, nwolfenb@utexas.edu

Abstract

The composition of impurities in ice controls the stability of liquid water and thus the distribution of potential aqueous habitats. We present a framework for modeling the brine volume fraction in impure water ice as a polynomial function of temperature and bulk ice salinity, inspired by models originally developed for sea ice. We applied this framework to examine the distribution of brine within the thermally conductive layer of Europa's ice shell, considering binary (NaCl and $MgSO_4$) and multi-ion "analog" (Cl-dominated and SO_4-dominated) endmember impurity compositions. We found the vertical extent of brine in a conductive ice layer, expressed as a fraction of the total layer thickness, to be $< 12\%$ for NaCl, $< 2\%$ for $MgSO_4$, and $< 18\%$ for both the analog endmember impurity compositions, suggesting that the depth where brine is stable in an ice shell is more sensitive to composition when only two ionic species are present. For the same temperature and bulk ice salinity, the brine volume fraction is higher in a Cl-dominated ice shell than a SO_4-dominated ice shell. Pressure, governed by the ice thickness, was found to have only a minor effect on the vertical extent of brine within an ice shell, relative to temperature and bulk salinity. The minimum stable bulk ice shell salinity formed through freezing of an ocean was found to be insensitive to composition and ultimately governed by the magnitude of the assumed percolation threshold.

Plain Language Summary

When ice forms from salt water, salt is excluded from the ice causing the remaining liquid water to become more saline, forming brine. We developed a method to build models that estimate how much brineexists in ice at a certain temperature for a certain amount of salt. Because water is a necessary ingredient for life, places where brine exists in ice represent potential habitats. We applied our method to the ice shell of Jupiter's moon Europa, assuming the ice shell formed from an ocean. Two possible oceans made up of different types of dissolved salts were considered. We found that the depth where brine is stable in an ice shell is more sensitive to the type of salt when two ions are present than when four ions are present. When the salt is made mostly of chloride, a larger volume of brine exists than when the salt is made up mostly of sulfate. The thickness of the ice shell did not affect the percentage of the ice layer where brine existed as much as temperature or the amount of salt did. The type of salt in the ocean did not affect how much salt was retained in the ice.

1 Introduction

The presence of liquid water has long guided the search for life beyond Earth (Des Marais et al., 2008). Once thought to be confined to the "Goldilocks zone", vast oceans have been inferred to exist beneath the thick ice shells of moons in the outer solar system (Hand et al., 2020). Although these sub-ice oceans represent the most compelling potential habitats in the outer solar system (Shematovich, 2018), they are covered by ice shells that can range from kilometers to hundreds of kilometers thick (Soderlund et al., 2020). Impurities within the ice shell, such as salts, acids, or organic compounds, could allow for liquid water to remain stable at temperatures well below that predicted by the pressure-melting curve of pure water (Marion et al., 2003, 2005; Ruiz et al., 2007). These impurities support the formation of intra-ice shell brine pockets, which could represent potential habitats that might be more accessible than the sub-ice ocean (Kargel et al., 2000; Marion et al., 2003).

Estimating the distribution of brine in an ice shell represents an important step in studying the habitability of ocean worlds. The brine volume fraction governs a number of bulk ice thermophysical properties, such as density, thermal conductivity, specific heat capacity, and viscosity (Petrich & Eicken, 2017). These thermophysical properties in turn govern processes of surface-ice-ocean exchange (e.g., solid-state convection, subduction, diapirism), thought to be important for habitability (Soderlund et al., 2020). Because the brine volume fraction also governs bulk dielectric properties, building models for the distribution of brine in an ice shell represents critical context for interpretation of ice-penetrating radar data collected by the upcoming JUpiter ICy moons Explorer (JUICE) and Europa Clipper missions (Blankenship et al., 2009, 2018; Bruzzone et al., 2013). In this work we focus on modeling the distribution of brine in the ice shell of Jupiter's moon, Europa, although we note the approach can be applied to impure water ice of any composition.

Impurities are incorporated into Europa's ice shell either by accretion of oceanic material at the ice-ocean interface (endogenic) (Buffo et al., 2018; Zolotov & Shock, 2001; Wolfenbarger et al., 2022), or the introduction of material at the surface through impactors or implantation by Io's plasma torus (exogenic) (Carlson et al., 2009; Brown & Hand, 2013; Ligier et al., 2016; Hendrix et al., 2011). Whereas exogenic impurities are sulfur-dominated, the composition of endogenic impurities is less well constrained. Magnesium

sulfate salts detected at the surface were originally thought to be derived from the ocean due to their correlation with young features (McCord et al., 1998; Hibbitts et al., 2019). However, higher spectral resolution Earth-based measurements using the W. M. Keck Observatory challenged this interpretation, finding that although the magnesium may be endogenic, the sulfates were likely exogenic, suggesting that chlorides could be the dominant endogenic anion (Brown & Hand, 2013). Subsequent measurements using Earth-based telescopes revealed signatures of chloride salts correlated to resurfacing features, supporting an oceanic origin (Trumbo et al., 2019; Ligier et al., 2016; Tan et al., 2022). Although observations of Europa's tenuous atmosphere suggest that sodium is the predominant cation, magnesium may still be abundant on the surface but inefficiently released into the atmosphere by sputtering (Ligier et al., 2016; Brown, 2001; Hörst & Brown, 2013). In this work we focus on endogenic impurities and leave exogenic impurities to future work. Ultimately, the composition of the ice shell resulting from entrainment of ocean material is governed by the composition of the sub-ice ocean, the rate of ice shell solidification, and processes operating within the ice shell that may promote fractionation, such as flushing by drainage of meltwater generated from tidal or shear heating (Wolfenbarger et al., 2022). As such, although we have constraints on the composition of surface impurities, there is still ambiguity to whether Europa's ocean is dominated by magnesium sulfate or sodium chloride salts.

Here we present a framework for modeling the brine volume fraction in ice, inspired by models developed for terrestrial sea ice (Sections 2.1 – 2.2). Whereas previous methods used data from a single freezing experiment to obtain properties of seawater brine as a function of temperature (Assur, 1960; Cox & Weeks, 1983), we employ the open source aqueous geochemistry program FREZCHEM to model the properties of multiple brines of different compositions (Marion & Kargel, 2007). We validate our approach by comparing against existing models for the brine volume fraction of sea ice (Section 2.3). For temperatures below the eutectic, brine is no longer stable; however, residual salts can serve as an indicator of relict water systems and thus as a signature of former potential habitats. As such we also consider the salt volume fraction and propose a model for its calculation in conjunction with brine volume fraction (Section 2.4). A method is proposed to account for the influence of pressure (Section 2.5). We adopt a linear temperature profile to represent both the case of a conductive lid overlying a convective ice layer and a thin, fully conductive ice shell (Section 2.6). A major motivation for the develop-

ment of the proposed framework is to facilitate the incorporation of more complex chemical species in geophysical investigations of ocean worlds. Application of this framework to ice shell models can ensure thermodynamic consistency is maintained without requiring direct integration with aqueous geochemistry software, which can introduce significant computational complexity and cost. By representing the chemical evolution of brine as it freezes using polynomial functions, we can translate the complex output of geochemistry software to a more broadly accessible, directly applicable form. This is an important step in facilitating multi-disciplinary research that is key to advancing the field of astrobiology.

We evaluate the distribution of thermodynamically stable brine for a thermally conductive ice layer of arbitrary thickness. Initially we consider two binary endmember compositions: NaCl and $MgSO_4$ (Section 3.1) before we increase the geochemical complexity and consider multi-ion systems with compositions more representative of natural waters that incorporate endmember compositions for Europa's ocean (Section 3.2). These more complex compositions are referred to as "analog" endmember compositions and represent a chloride-dominated and a sulfate-dominated Europan ocean. The influence of ice shell thickness (i.e., pressure) on the vertical extent of brine for the assumed linear temperature profile is examined for the analog endmember compositions (Section 3.3). The role of composition in governing bulk ice shell salinity is explored (Section 3.4), motivated by previous studies which argued that the brine volume fraction at which brine drainage can no longer occur, (i.e., a percolation threshold), may represent a critical parameter (Buffo et al., 2020, 2021; Wolfenbarger et al., 2022).

2 Methods

Impure ice is a multiphase, multicomponent system made up of solid ice, solid salts, liquid water, dissolved salts (i.e., ions), and trapped gases. The volume of brine stable in ice is governed by the bulk salinity of the ice, the temperature, and the composition of the salts. Representing the brine volume fraction as a function of these parameters for a particular brine system requires knowledge of the phase behaviour (i.e., the concentration or mass of ionic species, brine, ice, and precipitates as a function of temperature). Methods developed to model the brine volume fraction in sea ice, which represents the most ubiquitous and well-studied form of saline ice on Earth, serve as a foundation to develop models for saline ice on other worlds.

2.1 Equations for Modeling the Brine Volume Fraction of Sea Ice

An equation for the brine volume fraction of sea ice as a function of temperature, T, can be obtained from the relationships presented in Cox and Weeks (1983) (see SI 1.1) and is given by

$$\frac{V_b}{V}(T) = \left(1 - \frac{V_a}{V}(T)\right) \frac{\rho_i(T)S}{F_1(T) - \rho_i(T)SF_2(T)}, \tag{1}$$

where $\frac{V_b}{V}$ is the brine volume fraction, $\frac{V_a}{V}$ is the gas volume fraction, ρ_i is the density of pure water ice in units of g/cm^3, and S is the bulk salinity of the ice in units of ppt (i.e., weight percent expressed in g/kg solution). Note that for this work, we neglect the presence of trapped gases and assume $\frac{V_a}{V} = 0$. F_1 and F_2 are functions representing the properties of terrestrial seawater between the pure ice pressure melting temperature, T_m, and the eutectic temperature, T_{eut}. These phase behavior functions are defined as

$$F_1(T) = \rho_b(T)S_b(T)(1 + k(T)) \tag{2}$$

where ρ_b is the brine density in units of g/cm^3, S_b is brine salinity in units of ppt, and k is the ratio of the mass of solid salts (excluding bound water molecules) to the mass of dissolved salts in the brine, and

$$F_2(T) = (1 + C(T))\frac{\rho_b(T)}{\rho_i(T)} - \frac{C(T)\rho_b(T)}{\rho_{ss}(T)} - 1 \tag{3}$$

where ρ_{ss} is the density of solid salts (i.e., precipitates) in units of g/cm^3 and C is the ratio of mass of solid salts to the mass of brine. The original model of Cox and Weeks (1983), assumed a constant salt density of $\rho_{ss} = 1.5$ g/cm^3; however, here we use ρ_{ss} to represent the total salt density as a function of temperature (see SI 1.2). Note that the temperature dependence of ρ_{ss} represented here reflects the changing composition of salts, which are used to calculate the total density. We assume the density of an individual salt mineral is temperature invariant. The salt volume fraction can be expressed in terms of the brine volume fraction (where brine is stable) using an additional phase behavior function, which we define as F_3. The expression for the salt volume fraction is given by

$$\frac{V_{ss}}{V}(T) = F_3(T)\frac{V_b}{V}(T) \tag{4}$$

where $\frac{V_{ss}}{V}$ is the salt volume fraction, $\frac{V_b}{V}$ is the brine volume fraction, and

$$F_3(T) = C(T)\frac{\rho_b(T)}{\rho_{ss}(T)}. \tag{5}$$

Note that Cox and Weeks (1983) do not explicitly define a phase behavior function for the salt volume fraction as we do here, likely because the salt volume fraction is often negligible in sea ice applications.

These equations allow the brine volume fraction and salt volume fraction of impure water ice to be represented as a function of bulk ice salinity and temperature for the temperature range where brine is stable in the ice (i.e., from the pure ice pressure melting temperature to the eutectic temperature). Accordingly, the values of the phase behavior functions at the pure ice pressure melting temperature are $F_1(T = T_m) = 0$, $F_2(T = T_m) = \frac{\rho_w(T=T_m)}{\rho_i(T=T_m)} - 1$, and $F_3(T = T_m) = 0$, where ρ_w represents the density of pure water. Although these phase behavior functions are defined up to the pure ice pressure melting temperature, ice will not be stable at the pure ice pressure melting temperature for a bulk ice salinity greater than 0 ppt. The presence of salts will cause the freezing temperature to be lower than the pure ice pressure melting temperature (i.e., freezing point depression occurs when impurities are present).

A feature of this model is that the predicted brine volume fraction exceeds unity (non-physical) as the temperature increases beyond the freezing temperature for a specified bulk ice salinity. For example, this model predicts the brine volume fraction of 10 ppt sea ice will exceed unity at -0.054 °C which corresponds to the freezing temperature for 10 ppt terrestrial seawater. At temperatures which far exceed the freezing temperature, the model will transition from predicting brine volume fractions above unity to negative brine volume fractions (also non-physical). These non-physical brine volume fractions can be redefined as unity since they indicate conditions (temperature and bulk salinity) where ice is not thermodynamically stable and the solution is entirely liquid.

The phase behavior functions, F_1 and F_2, for terrestrial seawater were originally derived using the phase equilibrium table of Assur (1960), based off the experimental data of Nelson and Thompson (1954) and Ringer (1906). These experiments studied the phase

behavior as a function of temperature for a solution composition representative of standard terrestrial seawater. Although data were collected down to −54 °C, the phase behavior functions were only defined down to −30 °C, likely because this represented the temperature range of interest for terrestrial seawater. Later work using the open source aqueous geochemical modeling tool, FREZCHEM, demonstrated that the so-called Ringer-Nelson-Thompson (RNT) freezing pathway constructed by Assur (1960) may not be representative of the thermodynamically stable pathway for the freezing of terrestrial seawater (Marion et al., 1999). Instead, equilibrium freezing of terrestrial seawater appears to follow the experimental data of Gitterman (1937) which were unfortunately excluded from the work of Assur (1960) because the data were not available to him. More recent studies of the freezing of artificial sea ice brines have been consistent with the Gitterman pathway (Geilfus et al., 2013; Butler & Kennedy, 2015).

The major difference between these two pathways is the eutectic temperature, which is a consequence of the early precipitation of gypsum ($CaSO_4{\cdot}2H_2O$) along the Gitterman pathway (Marion et al., 1999). As a result of this, the Gitterman pathway reaches the eutectic at −36.2 °C with the precipitation of magnesium chloride dodecahydrate ($MgCl_2{\cdot}12H_2O$), whereas the RNT pathway reaches the eutectic at −53.8 °C with the precipitation of antarticite ($CaCl_2 \cdot 6H_2O$). Recent studies of both natural and artificial sea ice support that the Gitterman pathway best represents the equilibrium freezing of seawater (Geilfus et al., 2013; Butler & Kennedy, 2015; Butler, Papadimitriou, Santoro, & Kennedy, 2016; Butler et al., 2017; Butler, Papadimitriou, & Kennedy, 2016). Practically, this implies brine in sea ice is not thermodynamically stable below temperatures of −36.2°C. A detailed study of these two freezing pathways can be found in Marion et al. (1999).

Although FREZCHEM has been leveraged to study the equilibrium freezing of terrestrial seawater (Gitterman pathway) in a number of works since its inception (e.g., Vancoppenolle et al., 2019; Geilfus et al., 2013; Butler, Papadimitriou, Santoro, & Kennedy, 2016), the phase diagram of Assur (1960) (RNT pathway), is still the basis for modeling the brine volume fraction of sea ice (Petrich & Eicken, 2017). This could be responsible for introducing errors in estimates of sea ice brine volume fraction. For application to an ice shell, differences in eutectic temperatures resulting from freezing pathways and/or composition could translate to errors of up to a kilometer in predicted vertical brine extent as we will demonstrate in Section 3.1. This emphasizes the importance of accurately

representing the thermochemical dynamics of unique brine compositions in both geophysical and astrobiological investigations.

2.2 A Framework for Modeling the Distribution of Brine in Saline Ice

Although the equations in Section 2.1 were originally derived for application to sea ice, the approach is fundamentally agnostic to the solution composition, which can be represented by the phase behavior functions, F_1, F_2, and F_3. Furthermore, the advent of aqueous geochemistry software, such as FREZCHEM and PHREEQC, provides access to virtual laboratories where freezing experiments can be conducted for saline water on Earth and across the solar system (Marion & Kargel, 2007; Parkhurst et al., 2013). These software represent implementations of Pitzer models, where parameters derived from experimental data of binary or ternary salt solutions are extended to model more complex brine mixtures at different temperatures and pressures (Pitzer, 1991; Toner et al., 2015; Marion & Kargel, 2007; Parkhurst et al., 2013). These software are used extensively in planetary science, and have been applied to modeling brines on a number of worlds beyond Earth including Mars (e.g., Toner et al., 2014a, 2014b, 2015; Marion et al., 2013, 2016; Elsenousy et al., 2015), Europa (e.g., Zolotov & Shock, 2001; Marion et al., 2003, 2005; Kargel et al., 2000; Vance et al., 2019), Titan (e.g., Marion et al., 2012, 2014, 2015), and Enceladus (e.g., Marion et al., 2012; Fox-Powell & Cousins, 2021; Zolotov, 2007).

Because these virtual laboratories are built on estimated chemical parameters, they are subject to certain limitations imposed by the experimental data used to derive them. For example, the database that serves as the basis for FREZCHEM does not include thermal data (e.g., enthalpy and heat capacity), which could impact predictions at low temperature, or certain sulfate minerals, which could impact which mineral phase precipitates (Toner & Catling, 2017b, 2017a). A major limitation of FREZCHEM is that not all ion groupings have relevant Pitzer parameters and as such it is not internally self-consistent (Toner & Catling, 2017a). A new database developed for PHREEQC, ColdChem, improves on the database used in FREZCHEM by incorporating thermal properties and maintaining internal self-consistency; however, the database is currently limited to the Na-K-Ca-Mg-Cl-SO_4 system (Toner & Catling, 2017b, 2017a).

For this work we employ FREZCHEM version 15.1 for all freezing simulations with the exception of terrestrial seawater, where we use version 13.3. For terrestrial seawater, version 15.1 fails to converge where meridianiite should begin to precipitate and thus version 15.1 is unable to simulate freezing down to the eutectic temperature. We use FREZCHEM for this work, as opposed to the ColdChem database in PHREEQC, for the following reasons: (i) FREZCHEM outputs which salt mineral phases are likely to form at the eutectic temperature, beyond the final convergent temperature step, (ii) FREZCHEM includes carbonates, which allows us to model the freezing of terrestrial seawater, and (iii) ColdChem does not include molar volumes for solid phases, which prohibits the calculation of terms necessary for our framework, such as brine density and solid salt density. For the endmember compositions for Europa's ocean considered here, the salt precipitation sequence predicted by PHREEQC and FREZCHEM are comparable (see Table S7).

All FREZCHEM simulations were conducted assuming an initial temperature of 0 °C (273.15 K) and a temperature decrement of 0.1 K. An initial temperature of 0 °C was chosen to ensure that the onset of ice formation would be captured. We define the eutectic temperature as the temperature associated with the final convergent temperature step, as opposed to the temperature where FREZCHEM fails to converge. The parameters k, C, ρ_b, and S_b as a function of temperature can be derived from the FREZCHEM output file, which contains the solution composition and mineral phases at temperatures ranging from the initial temperature, specified in the input file, to the eutectic temperature, where the model no longer converges. The densities of solid salts are not directly output; however, molar volumes for each salt mineral are incorporated into the software and documented in the literature (Marion et al., 2005, 2012). These molar volumes are assumed to be independent of temperature and pressure. Temperature steps above the freezing point are excluded since they represent solution properties at a fixed salinity. Figure 1 presents a flowchart illustrating the framework for modeling the volume fraction of ice, brine, and solid salts leveraging the output of aqueous geochemistry software. We note that only a single freezing simulation is needed to obtain the phase behavior functions for a given composition, analogous to the single dataset which represents the basis for the phase behavior functions for terrestrial seawater.

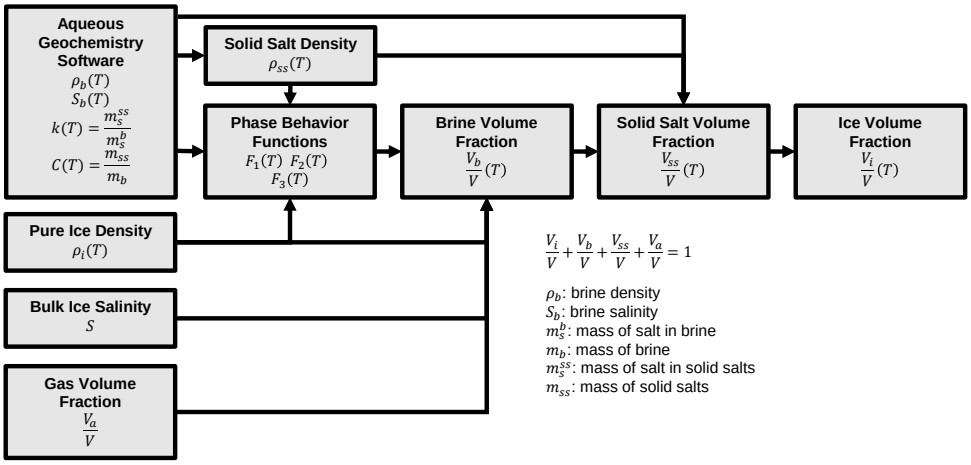

Figure 1. Flowchart describing our framework for modeling the volume fraction of brine and salt in saline ice.

A major advantage of this framework is that bulk ice salinity is decoupled from the composition of impurities. In other words, a single model derived for impure ice of a specified composition can be used to estimate the brine volume fraction for bulk ice salinities from infinite dilution to the eutectic salinity. However, to obtain the phase behavior functions for a specified composition, an initial solution concentration must be assumed. In the case of sea ice, recall that the original phase behavior functions were derived from experimental data from the freezing of 35 ppt terrestrial seawater. To examine the influence of the initial salinity on the phase behavior functions for a specified solution composition, we conducted a sensitivity study. Figure 2 illustrates the phase behavior functions derived from FREZCHEM simulations of terrestrial seawater (Millero et al., 2008) over a temperature range from 0 °C to −36.2 °C. The seawater salinity (i.e., the brine salinity specified in the FREZCHEM input file, corresponding to the brine salinity prior to any ice formation, $S_b(T = T_0)$) is varied to study the sensitivity of the phase behavior functions to the initial solution concentration. Note that the phase behavior functions shown here are truncated at the freezing temperature instead of extending to the pure ice pressure melting temperature, to show where the curves are overlapping. Although $F_2(T)$ and $F_3(T)$ are not influenced by the seawater salinity, $F_1(T)$ starts to exhibit appreciable differences when the salinity exceeds 100 ppt.

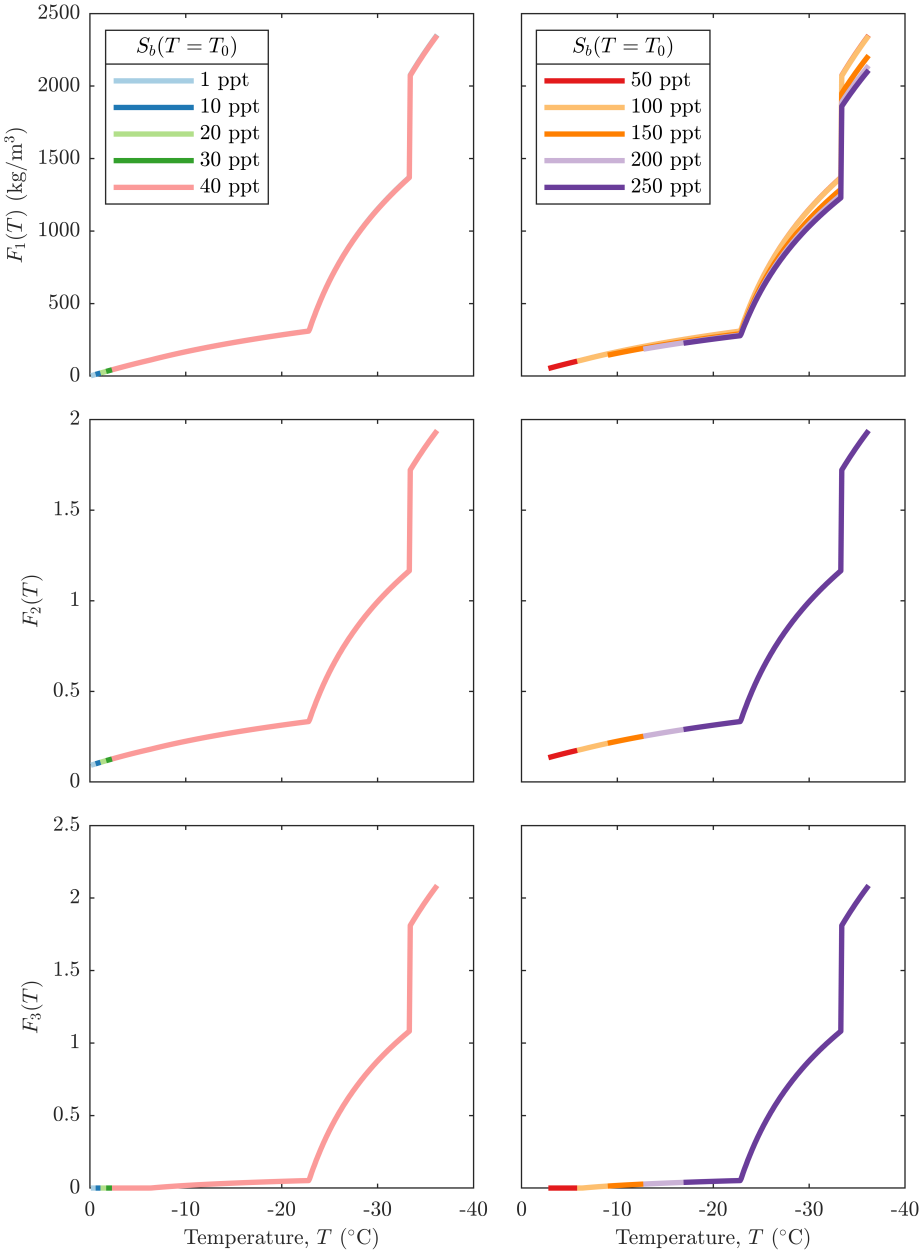

Figure 2. Phase behavior functions derived from FREZCHEM simulations of terrestrial seawater, assuming a range of initial seawater salinities $S_b(T = T_0)$.

The source of the discrepancy in $F_1(T)$ above 100 ppt can be attributed to the k term in Eq. (2). A higher k at a given temperature will cause a relative decrease in $F_1(T)$. Because k represents a quantification of salt precipitation normalized by the amount of dissolved salts in the brine, it is affected by changes in the salt precipitation sequence

(see Table S1). Below 100 ppt, the salt precipitation sequence is not influenced by the initial seawater salinity. Above 100 ppt, seawater is supersaturated with respect to certain salt minerals, specifically ikaite ($CaCO_3{\cdot}6H_2O$) for an initial seawater salinity $\geq$100 ppt, gypsum ($CaSO_4{\cdot}2H_2O$) for an initial seawater salinity $\geq$150 ppt, and mirabilite ($Na_2SO_4{\cdot}10H_2O$) for an initial seawater salinity $\geq$150 ppt. Supersaturation causes the salt to precipitate at the first temperature step in the FREZCHEM simulation ($T = 0°C$). The supersaturation of ikaite which occurs for an initial seawater salinity $\geq$100 ppt does not appear to noticeably affect $F_1(T)$, because the mass of ikaite which precipitates is negligible relative to the mass of dissolved salts in the brine. However for an initial seawater salinity $\geq$150 ppt, the combined mass of ikaite and gypsum precipitating at the first temperature step is no longer negligible relative to the mass of dissolved salts in the brine. Additionally, because the ion activities are higher at the first temperature step due to a higher initial concentration, a greater total mass of solid salts precipitate at the first temperature step, increasing k and thus decreasing $F_1(T)$ at every consecutive temperature step.

There are two important takeaways of the sensitivity study shown in Fig. 2 and Table S1: (i) the phase behavior functions are independent of the initial solution salinity, so long as the initial solution is sufficiently dilute (i.e., the solution is not supersaturated with respect to any salt) and (ii) the phase behavior functions are defined over a larger temperature domain for a lower initial solution salinity. Because terrestrial seawater has a salinity of approximately 35 ppt, the phase behavior functions were originally only defined for temperatures up to the freezing point of terrestrial seawater ($T_f \approx -2$ °C). The domain of the phase behaviour functions was eventually extended up to the pure ice pressure melting temperature of 0 °C (Leppäranta & Manninen, 1988), to represent more dilute solutions with relative compositions equivalent to terrestrial seawater (e.g., sea ice formed from the brackish waters of the Baltic Sea). This extension of the phase behavior functions to the pressure melting temperature amounts to interpolating the phase behavior functions between the freezing point to the pure ice pressure melting temperature. These extended phase behavior functions are analogous to the liquidus in simple binary systems. Brine density and brine salinity decrease to pure water as the temperature increases to the pure ice pressure melting point, and the brine density and brine salinity increase to the eutectic as the temperature decreases.

2.3 Validation through Comparison with Sea Ice

We validate our brine volume fraction model through comparison with the existing sea ice brine fraction model (Petrich & Eicken, 2017), originally obtained by Cox and Weeks (1983) and augmented by Leppäranta and Manninen (1988). We use FREZCHEM v13.3 to derive the phase behavior functions for terrestrial seawater, represented by the composition of Millero et al. (2008) in Marion et al. (2009). Figure 3 presents a comparison of the brine salinity, brine density, and phase behavior functions between the two models. The circles in the brine salinity curve are extracted directly from the phase equilibrium table of Assur (1960). The solid black curves in each plot depict the output of FREZCHEM. Note that because the FREZCHEM simulations are run for a specified impurity concentration (i.e., initial salinity), the phase behavior functions can only be defined from FREZCHEM output up to the solution freezing temperature, where ice begins to form (e.g., $T_f \approx -2$ °C for 35 ppt terrestrial seawater). To extend the domain of the phase behavior functions to the pure ice pressure melting temperature, we define an additional data point at the pure ice pressure melting temperature, corresponding to the value of the phase behavior functions for a brine salinity of zero and a brine density density equivalent to that of pure water (see Section 2.1). The black dashed curves depict the existing model for sea ice. The vertical dotted lines depict the temperatures at which salts begin to precipitate as the solution freezes. The thin red curves represent the phase behavior functions we derived by fitting piecewise polynomial functions of temperature to the FREZCHEM output (Table S2). Note that the functional form of our model is the same as existing model. The kinks in the phase behavior functions correspond to major precipitation events that occur along the freezing pathway, mainly the formation of hydrohalite ($NaCl{\cdot}2H_2O$) at −22.9 °C and meridianiite ($MgSO_4{\cdot}11H_2O$) at −33.3 °C. The brine density model used in the existing approach assumes a linear dependence of brine density on brine salinity, originally proposed by Zubov (1945), whereas our model extracts the brine density and brine salinity directly from the FREZCHEM output file.

Our model derived using FREZCHEM, presented in Table S2, agrees well with the existing model for temperatures above −22.9 °C, where hydrohalite begins to precipitate. For temperatures below −22.9 °C, our phase behavior functions exceed the existing model (Petrich & Eicken, 2017). This deviation is in part due to the underprediction of brine density in the existing model relative to that estimated by FREZCHEM.

An additional expected source of discrepancy is the freezing pathway represented in each model. Recall that modeling the equilibrium freezing of terrestrial seawater in FREZCHEM is consistent with the Gitterman pathway which more accurately represents the equilibrium freezing of terrestrial seawater than the RNT pathway assumed in the existing model. Our model extends the temperature domain where the brine volume fraction can be calculated for sea ice to below −30 °C. Although for Earth applications this temperature range may only be relevant under extreme conditions, defining the phase behavior functions over the entire temperature domain where brine is stable is critically relevant for application to the ice shells of ocean worlds.

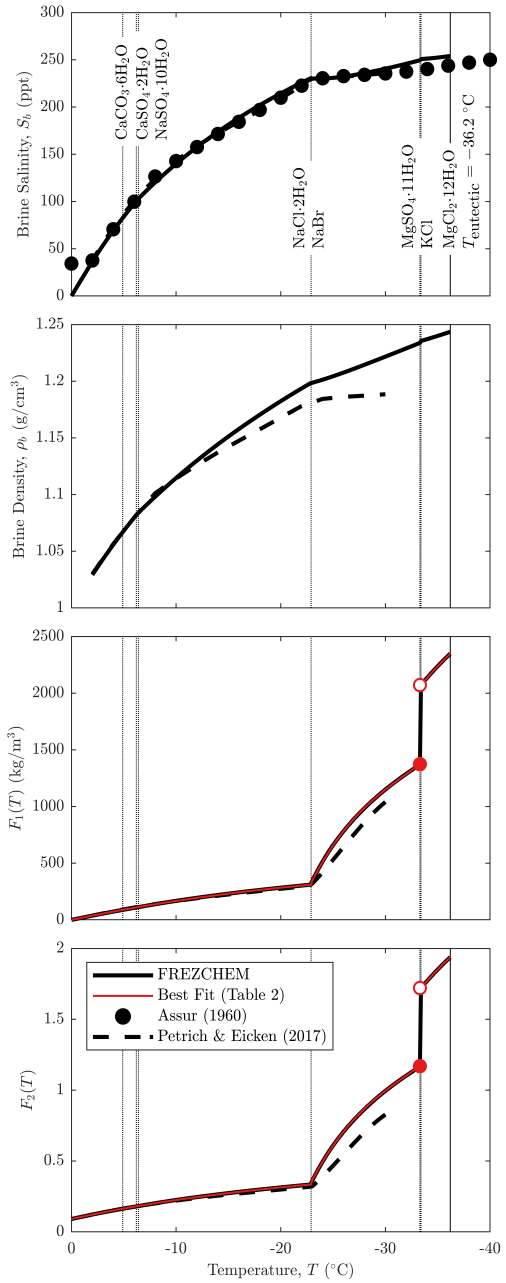

Figure 3. Validation of our framework through comparison of the phase behavior functions ($F_1(T)$ and $F_2(T)$), brine density (ρ_b), and brine salinity (S_b). The vertical dotted lines illustrate the temperature where a mineral (specified in the top panel) first begins to precipitate. The black solid curves represent values from FREZCHEM output, the black dashed curves represent the existing model of Petrich and Eicken (2017) that is based on the Assur (1960) dataset (denoted by black dots), and the thin red curves represent the model derived in this work (Table S2). Recall that curves derived from FREZCHEM are extended to temperatures above the freezing point of seawater to the pure ice pressure melting temperature, as described in Section 2.1.

Figure 4 presents a comparison of the brine volume fraction estimate for sea ice using our phase behavior functions in Table S2 and the phase behavior functions in the existing model of Petrich and Eicken (2017). $S = 5$ ppt is chosen because it represents a typical bulk salinity for sea ice and because of its significance to the "golden rule of fives", where at a bulk salinity of 5 ppt, the brine volume fraction is 5% at -5 °C (Golden et al., 1998). Instead of assuming a linear temperature dependence for the pure ice density term in Eq. (1), as is typically assumed (Petrich & Eicken, 2017), we use the equation of state for ice Ih released by the International Association for the Properties of Water and Steam (IAPWS) in IAPWS R10-06(2009), originally published by Feistel and Wagner (2006). We similarly use the equation of state for water released by the IAPWS in IAPWS SR7-09(2009), originally published by Feistel (2008), to obtain the density of water term needed to define $F_2(T = T_m)$ in Eq. (3). Similarly to Fig. 3, we use dotted lines to represent temperatures where salts begin to form as the solution freezes. Our estimated brine volume fractions are in good agreement with those predicted by the existing model for temperatures above -22.9 °C. The model of Petrich and Eicken (2017) predicts a slightly increased brine volume fraction at a given temperature relative to our model.

Importantly, both models are consistent with the "golden rule of fives", depicted as a yellow star in Fig. 4. The brine volume fraction of 0.05, often referred to as a critical porosity, is an important parameter in sea ice desalination models because it represents an apparent percolation threshold (Petrich et al., 2011; Turner et al., 2013; Buffo et al., 2018). Below a brine volume fraction of 0.05, convection-driven desalination no longer occurs due to a significant reduction in permeability (Golden et al., 1998, 2007; Pringle et al., 2009). This critical porosity applies to congelation sea ice, which is characterized by columnar ice crystals that grow parallel to the temperature gradient (Golden et al., 1998; Wolfenbarger et al., 2022). The agreement between our model and the existing model for sea ice (maximum deviation of 3.5% at approximately $T = -15$ °C and standard deviation of $< 2 \times 10^{-3}$ for $S = 5$ ppt) validates our approach; using aqueous geochemistry software to derive phase behavior functions to model the brine volume fraction of ice formed through the freezing of oceans on other worlds.

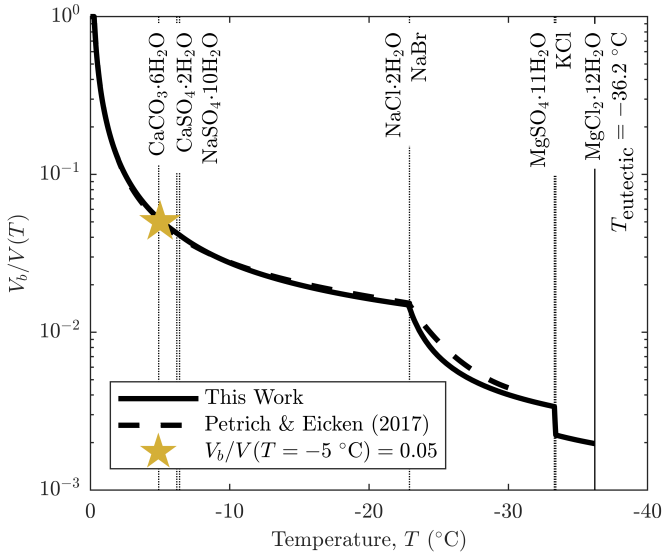

Figure 4. Brine volume fraction as a function of temperature for sea ice of bulk salinity $S = 5$ ppt. The vertical dotted lines illustrate the temperature where each mineral starts to precipitate. The solid curves represent the values derived in this work and the dashed lines represent the existing model. The yellow star illustrates the "golden rule of fives".

2.4 Estimating the Salt Volume Fraction below the Eutectic Temperature

Below the eutectic temperature (i.e., where brine is not thermodynamically stable), the salt volume fraction can be estimated using the expected mass fraction of solid salts at the eutectic temperature. Although FREZCHEM specifies which minerals are precipitating at/beyond the eutectic, it does not calculate the amount of each mineral precipitating. For a binary system (e.g., NaCl) estimating the mass fraction of solid salts at/beyond the eutectic is trivial since ions are contributing to only one non-ice mineral. For example, a 1 molal solution of NaCl, corresponding to a solution salinity of 55 ppt, will yield 1 mole of $NaCl{\cdot}2H_2O$, which translates to a solid salt mass fraction of 89 ppt. Because the mass of $NaCl{\cdot}2H_2O$ is higher than that of NaCl, the weight percent is higher. To obtain an estimate of the total mass of solid salts at/beyond the eutectic for more complex solutions, we must account for all salts which are precipitating (see SI 1.3). We define a scale factor, k^*, which represents the ratio of the total mass of solid salts at the eutectic, $m_{ss}(T \leq T_{eut})$, to the initial mass of dissolved salts in solution prior to any ice formation, $m_s^b(T = T_0)$ (i.e., $k^* = \frac{m_{ss}(T \leq T_{eut})}{m_s^b(T = T_0)}$). This scale factor is necessary be-

cause although the total mass of ionic impurities does not change as the solution freezes (i.e., mass is conserved), the salt minerals that precipitate can be hydrated (i.e., include bound water molecules). As such, the total mass of solid salts at the eutectic can exceed the initial mass of dissolved salts. k^* thus accounts for the hydration of all minerals that precipitate as the solution freezes, including those which form at/beyond the eutectic. To obtain an estimate of the salt volume fraction below the eutectic temperature, an estimate of the salt density is also needed. We calculate a total salt density, incorporating the estimate of solid salts formed at the eutectic, from the FREZCHEM output file. We can express the salt volume fraction in terms of these variables as

$$\frac{V_{ss}}{V}(T \leq T_{eut}) = \frac{Sk^*}{Sk^* + (1000 - Sk^*)\frac{\rho_{ss}(T=T_{eut})}{\rho_i(T)}} \tag{6}$$

where S is the bulk ice salinity in units of ppt and $\rho_{ss}(T = T_{eut})$ is the density of solid salts (i.e., precipitates) in units of g/cm^3 at the eutectic temperature.

2.5 Accounting for the Influence of Pressure

One limitation of our approach is that the pressure is assumed to be fixed (i.e., the pressure dependence of phase behavior is not modeled). This may not be an appropriate assumption for modeling the stability of brine where ice shells exceed a certain thickness, and the influence of overburden pressure is no longer negligible. One atmosphere of pressure, the pressure assumed in the brine volume fraction estimated for sea ice in Fig. 4, is the pressure equivalent to ∼100 meters of ice at Europa, which could represent <1% of the total ice shell thickness. Earlier work has studied the influence of pressure on brine chemistry, specifically with application to Europa (Marion et al., 2005). Here we discuss how the phase behavior functions are affected by pressure.

To robustly account for the influence of pressure for any solution, the phase behavior functions must be represented as a surface instead of a curve (i.e., a function of both temperature and pressure instead of solely temperature). The surfaces are generated from multiple FREZCHEM simulations for a given composition, where the pressure specified in the input file is varied over the pressure range of interest. Figure 5 is a graphical representation of the phase behavior surfaces for terrestrial seawater. These surfaces were generated using seven FREZCHEM simulations, assuming pressures of 1, 10, 100, 200,

300, 400, and 500 bar. Note that for a pressure of 1 atm, the surfaces would collapse to the curves in Fig. 3.

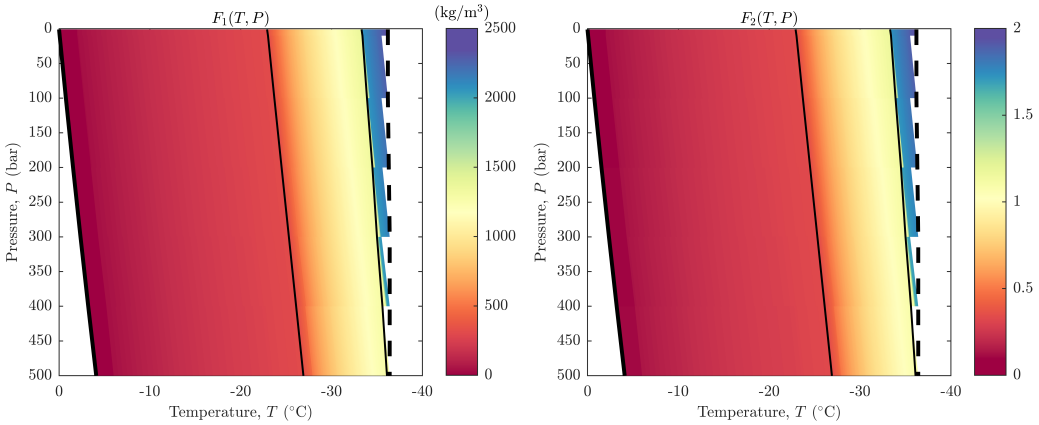

Figure 5. The surfaces defining the phase behavior functions for terrestrial seawater. The solid black curve represents the pure ice pressure-melting temperature and the dashed black curve represents the eutectic temperature. The thin black curves are where meridianiite and hydrohalite first begin to form, with hydrohalite forming at a higher temperature than meridianiite.

2.6 Temperature Profile

To model the distribution of brine within Europa's ice shell for an assumed composition, a temperature profile must also be assumed. The thermal state of Europa's ice shell is unknown; however, studies have shown that the ice shell is either convective, likely in the stagnant lid regime, or fully conductive (Mitri & Showman, 2005; McKinnon, 1999; Hussmann & Spohn, 2004). We note that early studies of heat transfer in Europa's ice shell constrained the maximum thickness for a conductive ice shell to be approximately 30 km (Ojakangas & Stevenson, 1989; Squyres et al., 1983). Later works incorporating the influence of convection estimate a maximum thickness ∼10 km for either a conductive lid or conductive ice shell, due to the onset of convection for thicker ice shells (McKinnon, 1999; Deschamps & Sotin, 2001; Kalousová et al., 2017; Tobie et al., 2003; Howell, 2021). The recent Monte Carlo analysis performed by Howell (2021) suggests a current best estimate for conductive ice layer thickness of $10.4^{+5.8}_{-1.9}$ km. For this work we assume a conductive temperature profile to represent both the case of a fully conductive ice shell and a conductive lid overlying a convective layer (Fig. 6).

Previous work has shown that the temperature of the convective layer is likely above the eutectic temperature for many salts, suggesting that brine is likely stable throughout the convective layer (Kalousová et al., 2017). Other works have demonstrated that even in the absence of salts, partial melting driven by tidal heating could be pervasive throughout a convective layer (Tobie et al., 2003; Vilella et al., 2020). The tendency for convection to increase the temperature of a large fraction of the ice shell, as well as to modify the ice rheology through deformation-induced recrystallization (Barr & McKinnon, 2007), could enhance brine drainage relative to an overall cooler conductive lid that might retain the columnar crystal structure characteristic of a directionally thickening ice layer (Wolfenbarger et al., 2022). If brine drainage is efficient throughout a convective layer, the layer will progressively desalinate and trend towards pure ice. As such we assume the same basal temperature for both the conductive lid and the conductive ice shell. To model a scenario representative of the maximum vertical brine extent, we thus assume (i) a surface temperature of -173.15 °C (100 K), approximately equal to the mean annual equatorial surface temperature at Europa, (ii) a basal temperature of 0 °C (273.15 K), the maximum pressure-melting temperature across a range of possible conductive ice layer thicknesses, and (iii) a linear temperature profile. Assuming a basal temperature of 0 °C implies the brine volume fraction will be unity for some fraction of the ice layer if the pressure exceeds 1 atm or the bulk salinity is greater than 0 ppt. In other words, part of our domain can include the uppermost layer of the ocean.

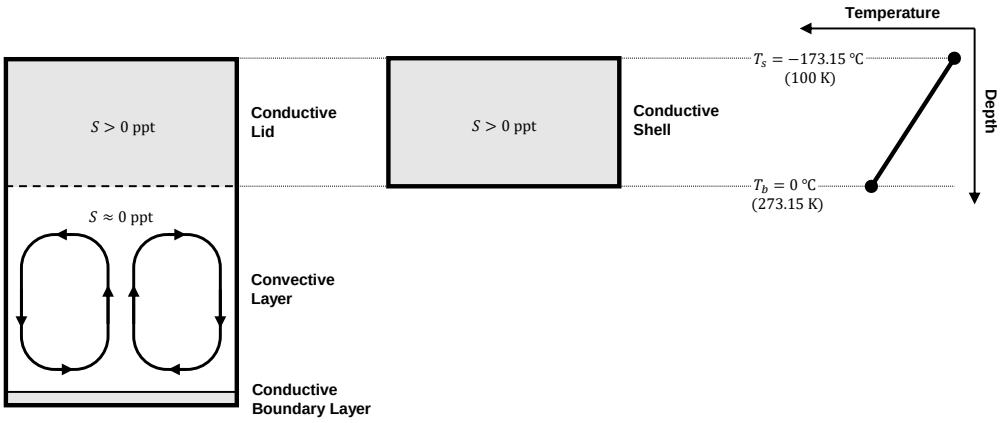

Figure 6. Temperature profile for the conductive layer of Europa's ice shell. The assumed profile applies to both the case of a conductive lid overlying a convective layer and a conductive ice shell. The surface temperature, T_s, basal temperature, T_b, and linear profile represent a specific hypothesis that maximizes the vertical brine extent within the ice shell.

3 Results

We model the brine volume fraction in Europa's ice shell as a function of temperature and salinity for four cases: 1) NaCl, 2) $MgSO_4$, 3) a hypothetical Cl-dominated ocean, and 4) a hypothetical SO_4-dominated ocean. Cases 1 and 2 represent the simple binary endmember compositions for Europa's ocean; whereas, cases 3 and 4 represent more realistic endmember compositions inspired by existing geochemical models, consistent with materials observed at Europa's surface. The Cl-dominated ocean is a simplified version of terrestrial seawater (Millero et al., 2008) and the SO_4-dominated ocean is a simplified version of the Europa K1a model of Zolotov and Shock (2001), both described in Table 1. We consider a range of bulk ice salinities, up to the eutectic salinity, assuming a fixed pressure of 1 atm. Recall that we assume a linear temperature profile such that the surface temperature is −173.15 °C (100 K) and the basal temperature is 0 °C (273.15 K) (see Section 2.6). Assuming the existence of a percolation threshold, constraints on bulk ice salinity are obtained both for sea ice and for the four cases of ice shell composition. We then analyze the sensitivity of brine volume fraction estimates to total conductive ice layer thickness (i.e., pressure), assuming a fixed bulk salinity of 1 ppt.

3.1 Binary Endmember Ice Shell Compositions

Figure 7 presents the brine and salt volume fraction of binary endmember compositions for Europa's ice shell: NaCl (left) and $MgSO_4$ (right). The maximum allowable bulk ice salinity is defined by the eutectic salinity (232 ppt for NaCl and 172 ppt for $MgSO_4$). We impose this constraint since the bulk ice salinity cannot exceed the eutectic salinity via cryoconcentration for binary systems. The phase behavior functions used to calculate the brine volume fraction are provided in Table S3. For estimating the salt volume fraction below the eutectic, we find $k^* = 1.6165$ and $\rho_{ss}(T = T_{eut}) = 1.630$ g/cm^3 for NaCl and $k^* = 2.6463$ and $\rho_{ss}(T = T_{eut}) = 1.446$ g/cm^3 for $MgSO_4$. Note that because these are binary solutions, the solid salt density at the eutectic simply corresponds to the density of hydrohalite and meridianiite for NaCl and $MgSO_4$, respectively. The thick dashed line illustrates the eutectic temperature and the thick solid curve represents the liquidus (i.e., the temperature above which the brine volume fraction is unity for a given bulk ice salinity). The thin dotted line indicates the temperature where the brine volume fraction first exceeds 0.05 for a given bulk ice salinity (see Section 3.4). Below the eutectic temperature the ice shell is composed of solid salt (hydrohalite for NaCl and meridianiite for $MgSO_4$) and ice, whereas above the eutectic temperature the ice shell is composed of brine and ice. Note that for binary solutions, if the bulk ice salinity is less than the eutectic salinity, the salt volume fraction is zero for temperatures greater than the eutectic temperature.

The vertical extent of brine is greater for NaCl than for $MgSO_4$ due to its lower eutectic temperature. For a 10 km conductive ice layer, this difference in eutectic temperature translates to a 1 km difference in vertical brine extent. Coincidentally, the difference in eutectic temperature between NaCl and $MgSO_4$ predicted by FREZCHEM v15.1 is approximately equal to that between the Gitterman and RNT freezing pathways for terrestrial seawater (see Section 2.1). For both compositions, the maximum brine volume fraction at the eutectic increases as the bulk ice salinity increases. Although the eutectic salinity of NaCl is higher than $MgSO_4$, because the density of hydrohalite is greater than meridianiite (1.63 g/cm^3 vs. 1.44 g/cm^3, respectively) the maximum salt volume fraction of NaCl is lower than $MgSO_4$ ($\sim$0.25 vs. $\sim$0.35, respectively).

Although we are able to estimate the brine volume fraction for bulk ice salinities up to the eutectic salinity, the bulk salinity of Europa's ice shell is limited by the effi-

ciency of salt entrainment from the ocean (Wolfenbarger et al., 2022; Buffo et al., 2020). The bulk salinity of Europa's ice shell resulting from equilibrium freezing of the ocean has been estimated to be as low as $\sim$ 0.1% and as high as $\sim$ 10% of the ocean salinity depending on the mechanism of ice formation and the microstructural interface morphology (Wolfenbarger et al., 2022). More locally, cryoconcentration of perched lakes or sills could generate regions of enhanced bulk salinity up to the eutectic salinity (Chivers et al., 2021). Rapid freezing of ocean water, such as through rifts in the ice shell, could also locally increase the bulk ice salinity (Buffo et al., 2020; Wolfenbarger et al., 2022). The salinity of ice formed via flash freezing of ocean water, such as the ice found in the Enceladus plume, could be as high as the salinity of the ocean (Postberg et al., 2011; Wolfenbarger et al., 2022). As such, in Figures 7 and 8, we estimate the brine volume fraction for the full possible parameter space of bulk ice salinity.

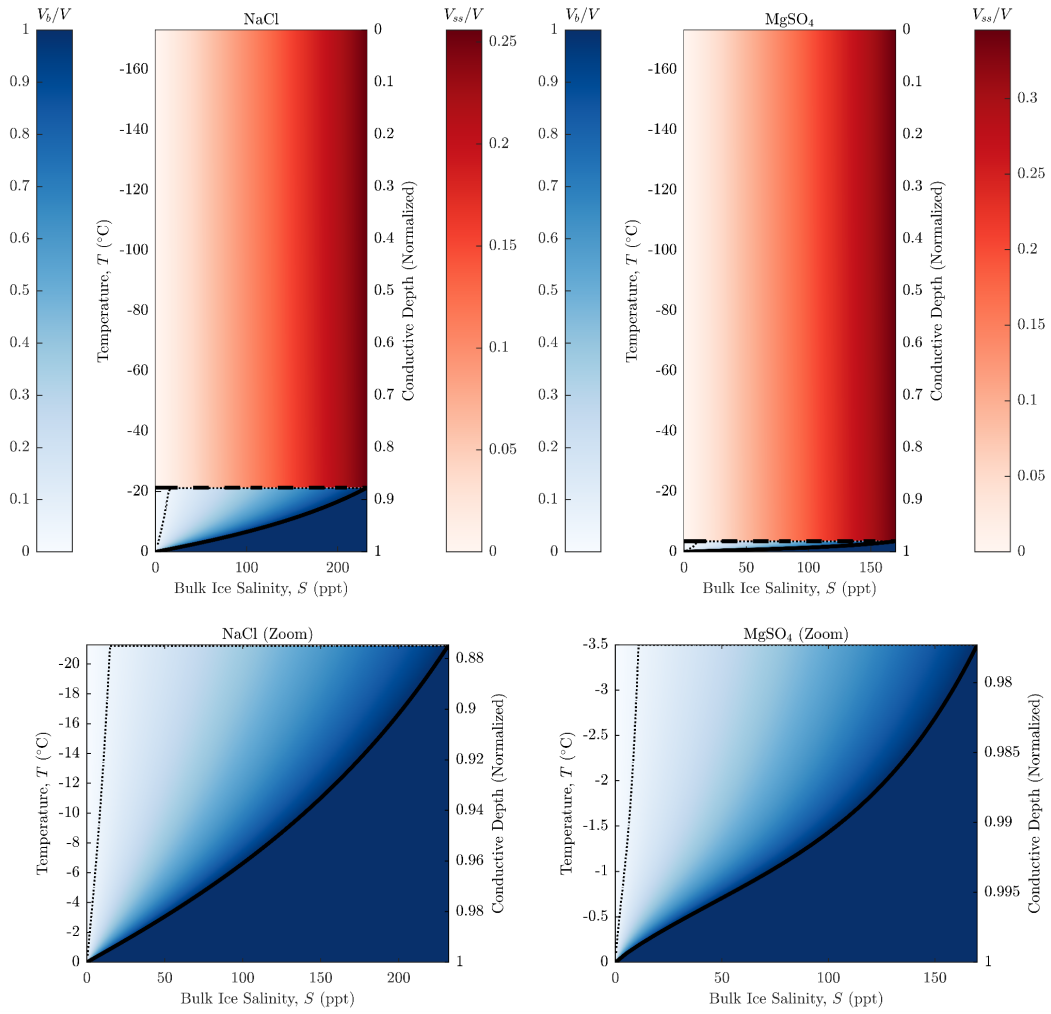

Figure 7. Brine volume fraction for Europa's ice shell assuming binary endmember compositions for the ocean and a fixed pressure of 1 atm. The vertical axis corresponds to the temperature at a given depth within the ice shell. The thick dashed line illustrates the eutectic temperature and the thick solid curve represents the brine salinity as a function of temperature (i.e., the liquidus). The thin dotted curve corresponds to a brine volume fraction of 0.05.

3.2 Analog Endmember Ice Shell Compositions

Although the cases considered in Fig. 7 are representative of the endmember compositions hypothesized for Europa, because the eutectic temperatures differ by almost an order of magnitude, the influence of composition on the distribution of brine is significant. The sensitivity to composition in the binary case likely does not represent the reality at Europa, where multiple salt minerals and ionic species have been detected at

the surface and in the tenuous atmosphere (e.g., Brown, 2001; Brown & Hand, 2013; Ligier et al., 2016; Trumbo et al., 2019; Fischer et al., 2015; Tan et al., 2022). Where multiple ionic species are present in a brine, precipitation events alter the brine composition such that it becomes progressively enriched in more soluble species (which precipitate at lower temperatures/ higher concentrations) as the solution freezes. For example, we expect a sulfate enriched brine to become progressively more enriched in chlorides since sulfates salts tend to precipitate at higher temperatures than chloride salts. We thus consider compositions that are more representative of natural waters, simplified to four major ionic species (Na^+,Cl^-,Mg^{2+}, SO_4^{2-}). Of the many possible charge-balanced permutations of these species, two compositions were selected because (i) they share the same eutectic temperature in FREZCHEM v15.1 of -32.2 °C (i.e., the vertical brine extent is the same) and (ii) they are analogous to known (Earth) or modeled (Europa) oceans. We note that the other charge-balanced permutations of these species resulted in eutectic temperatures of either -32.2 °C or -35.3 °C in FREZCHEM v15.1. Our Cl-dominated case is analogous to the terrestrial seawater composition of Millero et al. (2008), whereas our SO_4-dominated case is analogous to the Europa K1a ocean modeled by Zolotov and Shock (2001).

The compositions of the two analog endmember oceans are provided in Table 1. For this work we assume the ice shell composition reflects that of the ocean, leaving fractionation to a future work. The concentrations in Table 1 were obtained by approximating the relative concentrations of Zolotov and Shock (2001) and Millero et al. (2008), maintaining charge balance, and fixing the total concentration to 0.1 molal (i.e., ensuring the starting solution is relatively dilute). Table 1 also identifies which salts precipitate as the solutions freeze, as well as the temperature at which they begin precipitating. The differences in the salt precipitation sequence between these two compositions can be attributed to the relative abundances of the ions. In both cases the ion activity product of sodium and sulfate becomes sufficiently high and exceeds the equilibrium constant at relatively high temperatures, triggering mirabilite precipitation. This occurs at a higher temperature in the SO_4-dominated case since the limiting ion (Na^+) has a higher relative abundance than the limiting ion in the Cl-dominated case (SO_4^{2-}). The subsequent precipitation of hydrohalite in the Cl-dominated case occurs because mirabilite serves as a sink of an already limited supply of sulfate, preventing the precipitation of meridianiite until later in the sequence when the solution becomes more cryoconcentrated and the ac-

595 tivity is sufficiently high to trigger meridianiite precipitation. In the SO_4-dominated case,
596 meridianiite precipitates at a much higher temperature since mirabilite precipitation is
597 sodium-limited, resulting in an abundance of free sulfate to trigger the precipitation of
598 meridianiite. The formation of hydrohalite in the Cl-dominated case and the formation
599 of meridianiite in the SO_4-dominated case represent the two most significant precipita-
600 tion events, from the perspective of relative mass of solid salts forming, and as such co-
601 incide to the breakpoints in the phase behavior functions (Table S4 and S5).

602 Figure 8 presents the brine volume fraction of the analog endmember compositions
603 for Europa's ice shell: Cl-dominated (left) and SO_4-dominated (right). The phase be-
604 havior functions used to calculate the brine volume and salt volume fraction are provided
605 in Table S4 and S5. For estimating the salt volume fraction below the eutectic, we find
606 $k^* = 1.8439$ and $\rho_{ss}(T = T_{eut}) = 1.5827$ g/cm^3 for the Cl-dominated case and $k^* =$
607 2.5175 and $\rho_{ss}(T = T_{eut}) = 1.456$ g/cm^3 for the SO_4-dominated case. Unlike the bi-
608 nary cases in Fig. 7, the salt volume fraction is non-zero above the eutectic temperature
609 and calculated using Eq. (4). Although the solid black curve in Fig. 8 also represents
610 the brine salinity as a function of temperature, it is not a true liquidus (defined as the
611 temperature above which a solution is entirely liquid) since salt minerals may be stable
612 at higher temperatures if the solution salinity is sufficiently high. Recall that this is not
613 an issue for binary solutions since salts only precipitate via cryoconcentration at the eu-
614 tectic. As such for temperatures above this "pseudo-liquidus", the brine volume fraction
615 may be non-unity and salt volume fraction may be non-zero. Similarly, although we de-
616 fine the upper bound of our salinity domain as the brine salinity at the eutectic temper-
617 ature, this likely does not represent the maximum possible bulk ice salinity since solid
618 salts are also present in the brine at the eutectic salinity. This upper bound is likely only
619 relevant for cryoconcentrated, refrozen sills (Chivers et al., 2021).

620 Like the binary cases in Fig. 7, the thick dashed line illustrates the eutectic tem-
621 perature and the thin dotted line indicates the temperature where the brine volume frac-
622 tion first exceeds 0.05 for a given bulk ice salinity. The kinks in the brine salinity curves
623 indicate where significant salt precipitation events occur and cause the brine salinity to
624 decrease (e.g., hydrohalite for the Cl-dominated case at $T = -22.5$ °C and meridiani-
625 ite for the SO_4-dominated case at $T = -5.7$ °C). Our analog endmember compositions
626 suggest that brine is likely stable for a larger vertical extent in the ice shell than predicted
627 by simple binary compositions, regardless of which species are dominant ($< 18\%$ of the

conductive ice layer thickness for both the analog endmember impurity compositions vs. $< 12\%$ for NaCl and $< 2\%$ for $MgSO_4$). Although these analog endmember compositions share the same eutectic temperature, brine is present at a higher volume fraction throughout the Cl-dominated ice shell than the SO_4-dominated ice shell, whereas the opposite is true for salt volume fraction. The high brine volume fraction stable for the Cl-dominated ice shell is likely due to the late (i.e., at lower temperatures) precipitation of hydrohalite that occurs even when the activities of Na^+ and Cl^- are high, coupled with the fact that a much larger fraction of water is consumed by precipitation of meridianiite relative to hydrohalite (11 vs. 2 moles of water per mole of hydrate). Additionally, the tendency for sulfates to precipitate early (i.e., at higher temperatures) does not favor the stability of brine for the SO_4-dominated ice shell.

Table 1. Analog endmember compositions for Europa's ocean. The Cl-dominated case represents a simplified version of terrestrial seawater, whereas the SO_4-dominated case represents a simplified version of the K1a ocean of Zolotov and Shock (2001). Recall that $S_b(T = T_0)$ denotes the brine salinity specified in the FREZCHEM input file, and corresponds to the brine salinity prior to any ice formation. Note that it is the molar ratios that are important for the phase behavior functions and not the absolute concentrations (see Section 2.2 and Fig. 2).

	Cl-Dominated		SO_4-Dominated	
	Concentration (mol/kg)	Molar Ratio	Concentration (mol/kg)	Molar Ratio
Na^+	0.04390	43.9%	0.02308	23.1%
Mg^{2+}	0.00488	4.9%	0.03077	30.8%
Cl^-	0.04878	48.8%	0.00769	7.7%
SO_4^{2-}	0.00244	2.4%	0.03846	38.4%
Total	0.1		0.1	
$S_b(T = T_0)$	3.1 ppt		5.2 ppt	
	Salts Precipitating in FREZCHEM v15.1[a]			
	$Na_2SO_4{\cdot}10H_2O$	−6.1 °C	$Na_2SO_4{\cdot}10H_2O$	−3.4 °C
	$NaCl{\cdot}2H_2O$	−22.5 °C	$MgSO_4{\cdot}11H_2O$	−5.7 °C
	$MgSO_4{\cdot}11H_2O$[b]	−32.3 °C	$NaCl{\cdot}2H_2O$[b]	−32.3 °C

[a] See Table S7 for salt precipitation sequence predicted by using the frezchem and ColdChem database files in PHREEQC.

[b] FREZCHEM predicts this salt will precipitate beyond the final convergent temperature step, so we estimate this temperature as 0.1 °C below the eutectic temperature of −32.2 °C.

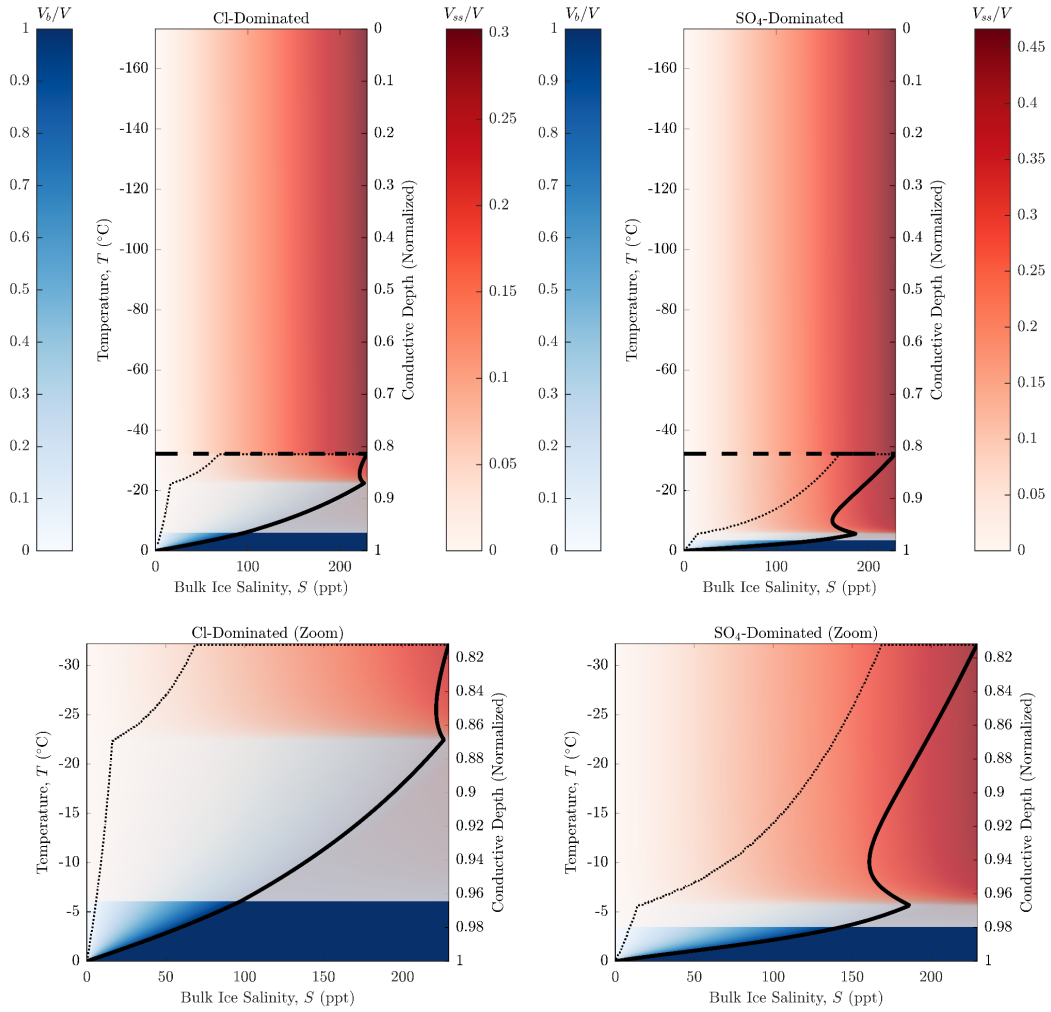

Figure 8. Brine volume fraction for a conductive ice layer at Europa assuming analog end-member compositions for the ocean and a fixed pressure of 1 atm. The vertical axis corresponds to the temperature at a given depth within the ice shell. The thick dashed line illustrates the eutectic temperature and the thick solid curve represents the brine salinity as a function of temperature. The thin dotted curve corresponds to a brine volume fraction of 0.05. The red color illustrating salt volume fraction is muted relative to the colorbar due to an imposed transparency which allows both the brine and salt phases to be visible where they are both stable between the eutectic and freezing temperature (see Fig. S3 for brine volume fraction alone).

3.3 Sensitivity to Pressure

Figures 7 and 8 represent the brine and salt distribution in an ice shell where overburden pressure is neglected and a fixed pressure of 1 atm is assumed throughout. We now incorporate the effect of ice thickness to examine the sensitivity of the distribution of brine to pressure. The influence of pressure is considered only for the analog endmember compositions and not the binary endmembers since the binary cases are more sensitive to pressure but are likely less realistic for a natural system.

Figure 9a presents the brine volume fraction for a 1 ppt conductive ice layer at Europa assuming analog endmember compositions for the ocean and a range of possible conductive layer thicknesses. 1 ppt represents an order of magnitude estimate for bulk ice salinity formed through freezing of a 10 ppt ocean (Wolfenbarger et al., 2022). The pressure at a given depth within the conductive layer is estimated by integrating the temperature-dependent ice density as a function of depth. Note that the conductive layer thickness shown in the figure legend applies to the entire temperature domain. Recall that we define the base of our domain as 0 °C (273.15 K) and as such (i) ice is not stable at this temperature for certain conductive layer thickness due to the reduction in pressure melting temperature and (ii) if the conductive ice layer overlies an ocean (as opposed to a pure ice convective layer) then the brine volume fraction curves will be truncated such that they equal unity below the ocean freezing temperature, which is governed by the ocean salinity.

Although the brine volume fraction curves shift upwards (lower in temperature) with increasing ice thickness, the general shape of the profile for each composition does not change significantly. This is highlighted in Fig. 9b where the brine volume fraction curves appear to overlap when they are plotted against the relative temperature, defined here as the difference between the absolute temperature (the y-axis in Fig. 9a) and the pure ice pressure melting temperature. This result is compatible with recent experimental work that demonstrated that the change in eutectic temperature of saline ice subject to pressure is well-approximated by the pure ice pressure melting curve (Chang et al., 2022). For both the analog endmember compositions, the eutectic temperatures (shown as the thin dashed lines in Fig. 9a) are not as sensitive to pressure as the melting temperature. As such, larger ice thicknesses translate to a lower vertical brine extent, defined as the fraction of the total conductive ice layer thickness where brine is thermo-

dynamically stable. For the range of conductive layer thicknesses considered here, Fig. 9c shows this effect is relatively minor (<1% of the conductive ice layer thickness), and the fraction of the conductive ice layer where brine is stable for the assumed temperature profile is between 18% and 19%. Note that for estimating the vertical brine extent, we recalculate the conductive layer thickness to ensure the ice is stable for the assumed thermal profile and pressure.

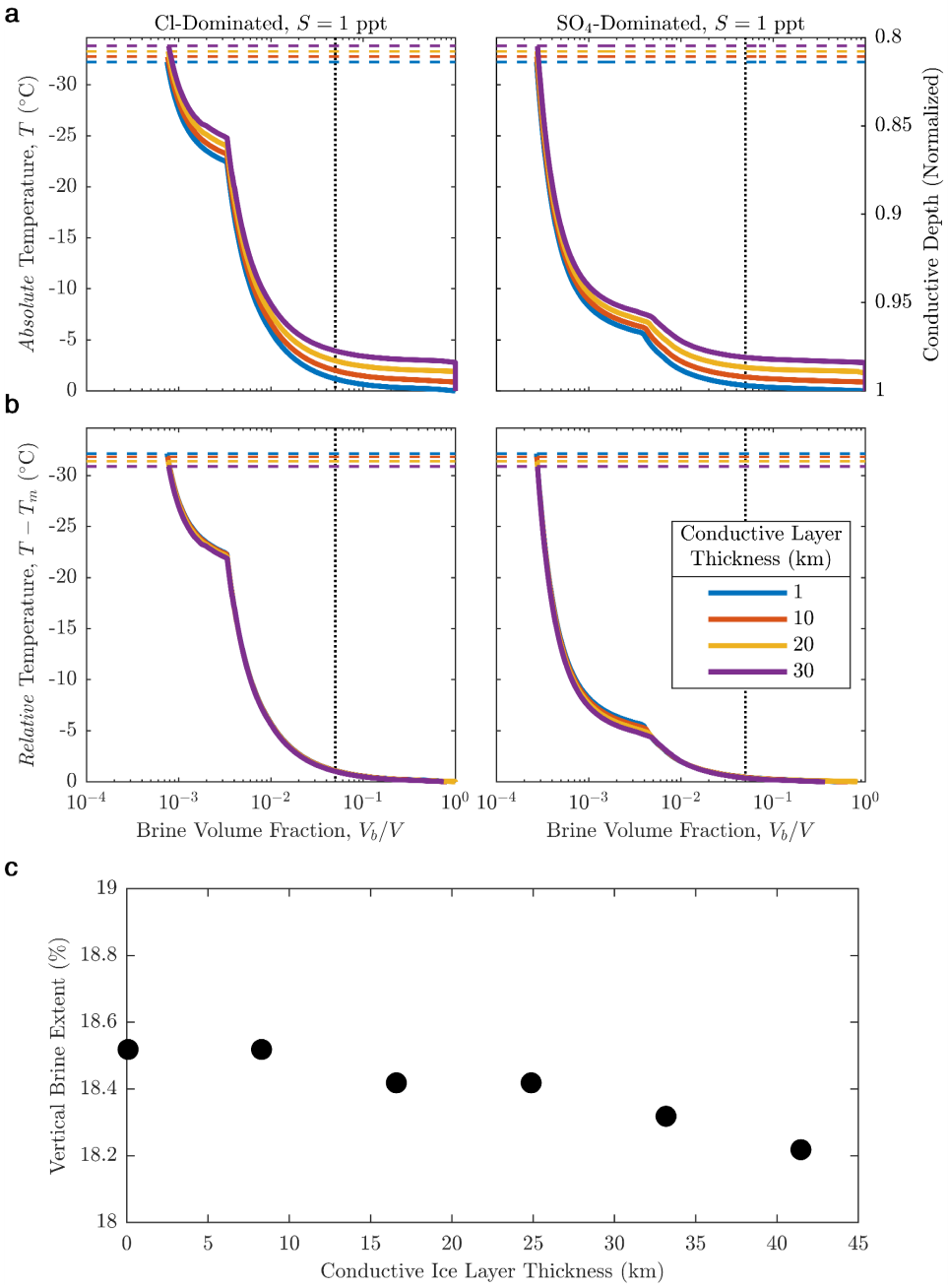

Figure 9. Influence of pressure on the distribution of brine in the bottom 20% of the conductive layer for our analog endmember compositions. (a,b) Brine volume fraction for a 1 ppt conductive ice layer at Europa assuming analog endmember compositions for the ocean and a range of possible conductive ice thicknesses. The thin, horizontal dashed lines represent the eutectic temperature for a given ice thickness. The thin, vertical dotted lines represent a brine volume fraction of 0.05 (see Section 3.4). The top row (a) shows the brine volume fraction for the conductive layer as a function of *absolute* temperature whereas the middle row (b) shows the brine volume fraction as a function of *relative* temperature, defined as the difference between the *absolute* temperature and the pure ice pressure melting temperature. (c) Fraction of the conductive ice layer where brine is stable as a function of conductive ice layer thickness for both analog endmember compositions .

3.4 Constraints on the "Stable" Bulk Ice Shell Salinity

Previous studies focused on constraining Europa's ice shell salinity have used inferences based on the assumption of brine pocket migration in an impact crater (Steinbrügge et al., 2020), numerical models developed for sea ice desalination (Buffo et al., 2020), or studied ice formed in environments that could be analogous to Europa's ice-ocean interface, such as ice accreted beneath terrestrial ice shelves in Antarctica (Wolfenbarger et al., 2022). The latter two studies demonstrated that the bulk salinity for an ice shell which forms through freezing of a sub-ice ocean should approach a lower limit referred to as the "asymptotic" bulk salinity in Buffo et al. (2020) and the "stable" salinity in Wolfenbarger et al. (2022).

In the model of Buffo et al. (2020), the asymptotic bulk salinity reflected an imposed cutoff in permeability (i.e., percolation threshold) at a brine volume fraction of 0.05, consistent with the critical porosity for congelation sea ice referenced in Section 2.3. The later work of Buffo et al. (2021) did not directly impose a percolation threshold, but used a permeability-porosity relationship derived for sea ice which exhibits significantly reduced permeability at brine volume fractions less than 0.05. Although some authors argue that the existence of a percolation threshold in sea ice prevents desalination for brine volume fractions below the critical porosity (Golden et al., 1998, 2007), others argue that the desalination mechanism transitions from an efficient convection-dominated process known as gravity drainage to a less efficient diffusion-dominated process (Buffo et al., 2020, 2021).

Wolfenbarger et al. (2022) examined the salinity profiles of low temperature gradient ice cores to obtain constraints on the fraction of salt entrained in ice formed through slow freezing of an ocean. They represented this fraction using an effective equilibrium solute distribution coefficient, defined as the ratio of the stable salinity of ice, derived from the salinity profiles, normalized by the salinity of the underlying ocean ($k_{eq} = S_{ice}/S_{ocean}$). Wolfenbarger et al. (2022) noted that there was a similarity between the value they derived for the effective equilibrium solute distribution coefficient and the critical porosity for congelation sea ice. They interpreted this similarity as evidence supporting that a percolation threshold likely governed the effective equilibrium solute distribution coefficient. Because the critical porosity reflects a volume fraction whereas the solute distribution coefficient represents a mass fraction, these quantities are not directly compa-

rable; however, our brine volume fraction model allows us to explore the relationship between these quantities while ensuring thermodynamic compatibility.

Figure 10a illustrates the dependence of sea ice brine volume fraction on bulk ice salinity and temperature. The region in blue signifies temperatures above the freezing point for 35 ppt terrestrial seawater. The dashed line represents the percolation threshold at a brine volume fraction of 0.05. Curves to the right of the dashed line, within the gray area, reflect ice that is still highly permeable, and thus presumably in an active state of desalination. Curves to the left of the dashed line are effectively impermeable and no longer undergoing convection-driven desalination. This plot suggests that the bulk salinity of newly formed sea ice subject to a percolation threshold of 0.05 cannot fall below approximately 2 ppt, since convection-driven desalination cannot occur below this salinity even at the warmest possible temperature where sea ice can form (i.e., the seawater freezing temperature).

Because sea ice forms in a high temperature gradient environment, salt entrainment is facilitated by the progression of a freezing front which traps brine interstitially and prevents continued drainage. As such, the stable bulk salinity of sea ice is typically higher than 2 ppt ($\sim$5 ppt). The arrows in Fig. 10a represent an illustration of a possible desalination pathway which produces sea ice with a stable bulk salinity of 5 ppt, adapted from Petrich and Eicken (2017). A higher temperature gradient freezing pathway would fall below the red curve, whereas a lower temperature gradient pathway would appear above the red curve.

Recognizing that brine drainage will outpace the freezing front at the very low growth velocities expected at Europa's ice-ocean interface (Wolfenbarger et al., 2022), we can leverage the existence of a percolation threshold to constrain the stable bulk ice shell salinity. The bulk ice salinity that results in a brine volume fraction equal to the critical porosity, at the ocean freezing temperature, represents a minimum bound for salt entrainment in ice where desalination is subject to a percolation threshold. This condition can be expressed mathematically using Eq. (1) to obtain

$$\phi_c = \frac{V_b}{V}(T_f(S_{ocean})) = \frac{\rho_i(T_f(S_{ocean}))S_{ice}}{F_1(T_f(S_{ocean})) - \rho_i(T_f(S_{ocean}))S_{ice}F_2(T_f(S_{ocean}))}, \tag{7}$$

where ϕ_c is the critical porosity (brine volume fraction) that defines the percolation threshold, T_f is the ocean freezing temperature, governed by the ocean salinity, S_{ocean}, and S_{ice} is the stable bulk ice shell salinity. Compatible with previous works, we first assume the percolation threshold occurs at a brine volume fraction of 0.05. As such, we consider the bulk ice salinity that results in a brine volume fraction of 0.05 at the ocean freezing temperature to represent the stable bulk salinity of the ice shell.

If we apply this criterion to terrestrial seawater at 35 ppt, we obtain a bulk ice salinity estimate of 1.95 ppt. This corresponds to the bulk salinity curve which intersects both the vertical dotted line and the horizontal lower boundary of the blue region in Fig. 10a. This is notably the bulk ice salinity obtained using the constitutive equation of Buffo et al. (2018) for the freezing of terrestrial seawater in the "diffusive regime" (i.e., where ice is transitioning to being effectively impermeable), although we note they assume a seawater salinity of 34 ppt. The bulk salinity of 1.95 ppt obtained here is lower than the bulk ice salinity found for the "sub-ice-shelf congelation ice" samples studied by Wolfenbarger et al. (2022), which ranged from 2.2 to 2.35 ppt. To produce a stable bulk ice salinity of 2.35 ppt using this methodology, a critical porosity of 0.06 would be required.

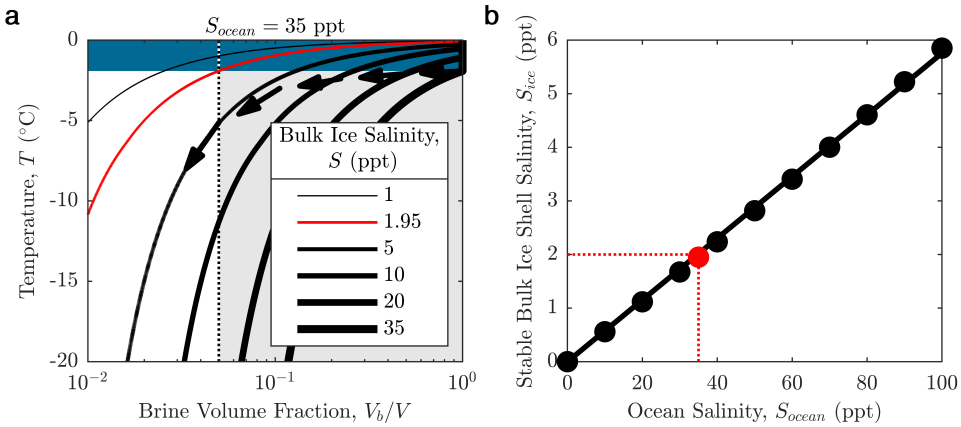

Figure 10. Relationship between brine volume fraction, bulk ice salinity, and ocean salinity for terrestrial seawater. (a) Brine volume fraction for sea ice assuming a range of bulk ice salinities, adapted from Butler (2016). The black arrows illustrate a possible desalination pathway. The red curve represents the stable bulk ice shell salinity derived for a 35 ppt ocean, assuming a percolation threshold ($\phi_c = 0.05$) (b) Stable bulk ice shell salinity for a range of possible ocean salinities. Data points correspond to the bulk ice salinity where the brine volume fraction equals the percolation threshold ($\phi_c = 0.05$) at a freezing temperature governed by ocean salinity, analogous to the red curve in a. The red dot represents the specific case of a 35 ppt ocean shown in a. The line represents a best fit model of the form $S_{ice} = k_{eq} \times S_{ocean}$, where $k_{eq} = 0.058 \pm 0.001$.

Using FREZCHEM, we can extend our analysis to more dilute and more saline terrestrial seawater. We use our brine salinity curve, shown in Fig. 3a, to obtain a freezing temperature for a specified seawater salinity. For seawater salinities up to 100 ppt (note that we limit the upper bound seawater salinity to 100 ppt to ensure our brine volume fraction model is valid, see Section 2.2), we can calculate the bulk ice salinity which produces a brine volume fraction of 0.05 at the freezing temperature. These bulk ice salinities are represented by the black dots in Fig. 10b. We can estimate an effective equilibrium solute distribution coefficient by fitting a linear model of the form $S_{ice} = k_{eq} \times S_{ocean}$. These data produce an estimate for an effective equilibrium solute distribution coefficient of $k_{eq} = 0.058 \pm 0.001$, represented by the slope of the line shown in Fig. 10b. We note this is lower than the value of 0.067 derived by Wolfenbarger et al. (2022). This might suggest a higher critical porosity should be assumed or that temperature where the percolation threshold is applicable should be slightly lower than the freezing temperature, even in the case of a very low temperature gradient.

If we further extend this approach to our analog endmember compositions, Fig. 11a shows that the effective equilibrium solute distribution coefficient is not highly sensitive to composition for ocean salinities less than 100 ppt (the ocean salinity range where our model is valid, see Fig. S1, S2 and Table S5). From a best fit model of the form $S_{ice} = k_{eq} \times S_{ocean}$, we obtain an effective equilibrium distribution coefficient of $k_{eq} = 0.058 \pm 0.001$ for a percolation threshold of $\phi_c = 0.05$ and ocean salinities less than 100 ppt. For the binary endmember cases, our model is valid for salinities up to the eutectic salinity and as such we can explore the full parameter space. Fig. 11b demonstrates that the behavior shown in Fig. 11a does not appear to change significantly when extended to eutectic ocean salinities. At higher salinities, the relationship between stable bulk ice shell salinity and ocean salinity appears to deviate slightly from linear. Nonetheless, we obtain an estimate for effective equilibrium distribution coefficient of $k_{eq} = 0.061 \pm 0.001$ which is similar to our analog endmember compositions, but still lower than the value of 0.067 derived by Wolfenbarger et al. (2022). Figure 11c demonstrates that the equilibrium solute distribution coefficient increases as the value of the assumed percolation threshold increases. This is consistent with the work of Buffo et al. (2020), where a lower percolation threshold was shown to result in less salt entrainment. Additionally, Fig. 11c suggests that the freezing of a SO_4-dominated ocean may produce slightly more saline ice than a Cl-dominated ocean ($k_{eq} = 0.116$ vs. $k_{eq} = 0.114$ for a percolation threshold of $\phi_c = 0.1$).

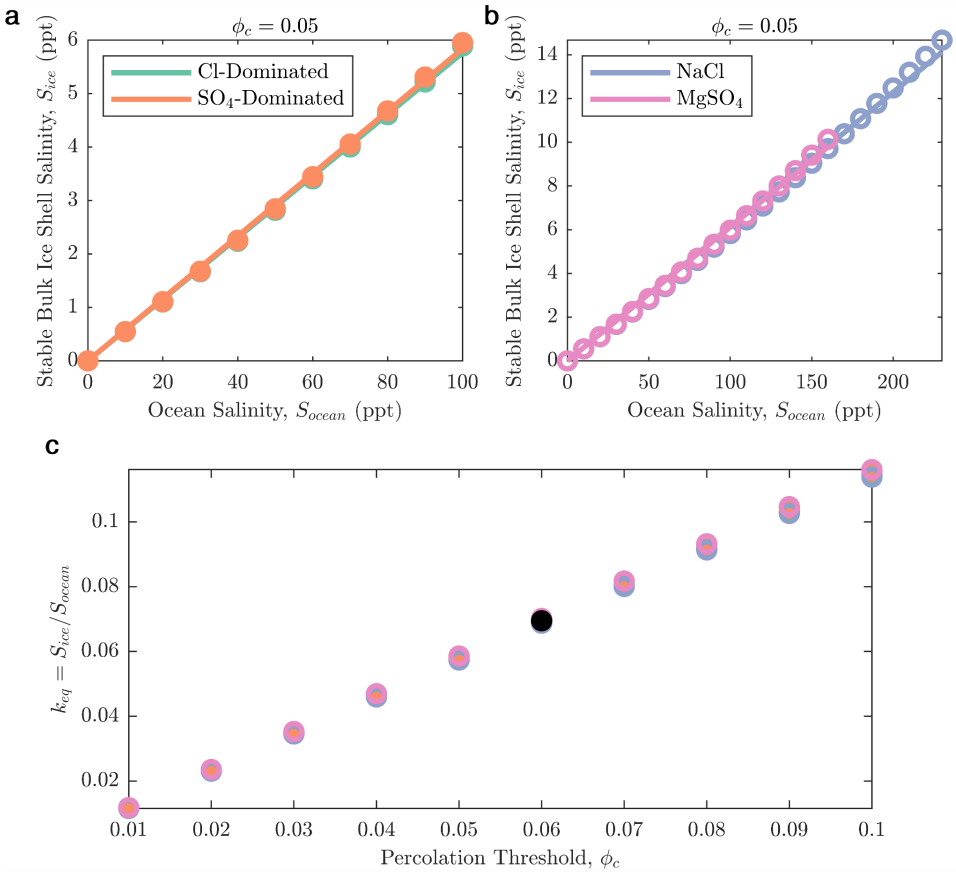

Figure 11. Relationship between bulk ice salinity, ocean salinity, and percolation threshold for a range of compositions. Estimates for bulk ice salinity as a function of ocean salinity for our (a) analog endmember compositions and (b) binary endmember compositions, based on a percolation threshold of $\phi_c = 0.05$. Data points correspond to the bulk ice salinity where the brine volume fraction equals 0.05 at a freezing temperature governed by the ocean salinity and composition. The lines represent a best fit model of the form $S_{ice} = k_{eq} \times S_{ocean}$, where $k_{eq} = 0.058 \pm 0.001$ for the analog endmember compositions and $k_{eq} = 0.061 \pm 0.001$ for the binary endmember compositions. (c) Effective equilibrium solute distribution coefficient for a range of percolation thresholds and different ocean compositions. The black dot represents the effective equilibrium distribution coefficient for a percolation threshold of $\phi_c = 0.060$, derived in this work from the "sub-ice-shelf congelation ice" samples studied by Wolfenbarger et al. (2022).

The magnitude of the percolation threshold in columnar sea ice has been demonstrated to be influenced by the interface morphology of the ice (i.e., the spacing between columnar crystals that make up the cellular microstructural interface) (Maus et al., 2021). Although we do not explore the influence of plate spacing on the critical porosity in this

work, previous studies suggest that the critical porosity should decrease as the plate spacing increases (Petrich et al., 2006; Maus et al., 2021). The plate spacing in congelation ice is inversely proportional to the growth velocity, such that a slower growth (i.e., lower temperature gradient) results in larger plate spacing (Maus, 2020; Maus et al., 2021). For the low growth velocities expected at Europa's ice-ocean interface (Wolfenbarger et al., 2022), this could translate to a lower critical porosity and thus lower bulk ice shell salinity. As the growth velocity approaches zero, the plate spacing approaches infinity and transitions from a cellular to planar microstructural interface morphology. This transition enhances the efficiency of salt rejection and results in an even lower bulk ice shell salinity (Wolfenbarger et al., 2022). These results suggest that constraining the existence and magnitude of a percolation threshold in columnar ice (i.e., critical porosity) represents a critical step in both predicting the bulk salinity of the ice shell and leveraging the bulk salinity of the ice shell to constrain the salinity of the underlying ocean.

4 Conclusions

We have developed a framework for modeling the brine volume fraction of impure water ice as a function of bulk ice salinity and temperature. In this framework we translate the output of a single freezing simulation for a specified ocean composition (performed using the open source aqueous geochemistry software FREZCHEM) to polynomial functions of temperature. We validated our framework through comparison with an existing model for sea ice brine volume fraction (Petrich & Eicken, 2017), finding good agreement over the range relevant to Earth applications. Our model represents an improvement to the existing model by (i) extending the temperature range where sea ice brine volume fraction can be estimated down to the eutectic temperature and (ii) following the Gitterman freezing pathway, thought to be more representative of natural sea ice (Marion et al., 1999). Although we apply our framework specifically to Europa, models for the brine volume fraction of impure water ice can be derived for any system that can be modeled using aqueous geochemistry software, such as FREZCHEM or PHREEQC. Notably, these models can be continually improved as new experimental data are incorporated into geochemical modeling databases.

Within our framework, we generated models for the brine distribution in Europa's ice shell, specifically focusing on the fraction which is thermally conductive (either a conductive lid overlying a convective layer or a fully conductive ice shell). We assumed a

linear temperature profile that maximized the vertical brine extent. As such our estimates for vertical brine extent represent upper bounds for what is expected at Europa. We modeled the brine volume fraction for four cases of ice shell compositions, consistent with materials observed at Europa's surface: NaCl, $MgSO_4$, a hypothetical Cl-dominated ocean (analogous to terrestrial seawater), and a hypothetical SO_4-dominated ocean (analogous to the Europan ocean modeled by Zolotov and Shock (2001)), and considered bulk ice salinities ranging from zero to the eutectic salinity.

We found the vertical extent of brine in an ice shell to be $< 12\%$ for NaCl, $< 2\%$ for $MgSO_4$, and $< 18\%$ for both the analog endmember impurity compositions. Where impurities are composed of binary species (e.g., Na^+ and Cl^- or Mg^{2+} and SO_4^{2-}), the vertical brine extent is confined to lower depths (i.e., closer to the ice-ocean interface), a smaller fraction of the ice layer thickness, and more sensitive to composition than an ice shell where impurities are composed of multiple species (e.g., Na^+, Cl^-, Mg^{2+} and SO_4^{2-}). Although the vertical extent of brine was equivalent for the two analog endmember compositions (because they shared a eutectic temperature), the brine volume fraction for the Cl-dominated ice shell was higher than for the SO_4-dominated ice shell across the entire temperature range where brine was thermodynamically stable. Pressure (ice thickness) was found to minimally affect the shape of the phase behavior functions, and thus brine distribution profile; however a larger ice thickness was found to counter-intuitively reduce the fraction of the ice layer where brine is stable although the effect was minor ($\sim 1\%$) across a range of possible thickness.

Assuming the existence of a percolation threshold at a brine volume fraction of 0.05 (consistent with the broadly accepted value for terrestrial congelation sea ice), constraints on the stable bulk ice shell salinity (i.e., the salinity of the ice shell once desalination has stopped) as a function of ocean salinity and composition were obtained. We defined the stable bulk ice shell salinity to be the bulk ice salinity that resulted in a brine volume fraction equal to the percolation threshold at the ocean freezing temperature. The stable bulk ice shell salinity was found to be approximately 6% of the ocean salinity for the assumed percolation threshold. The relationship between percolation threshold and the effective equilibrium solute distribution coefficient was found to be approximately linear, positively correlated, and minimally influenced by composition for critical porosities considered here ($\phi_c = 0.01 - 0.1$).

Modeling where brine is thermodynamically stable in Europa's ice shell provides important context for future interpretation of data collected by the upcoming missions to explore Europa and other icy worlds (Howell & Pappalardo, 2020; Grasset et al., 2013). Ice-penetrating radar in particular can identify where liquid water is stable in the ice shell. With improved constraints on ice shell surface composition and temperature, reflections from ice-penetrating radar associated with a eutectic boundary may provide constraints on bulk ice shell properties, such as the thermal profile (Kalousová et al., 2017) and/or salinity, particularly because the apparent reflectivity is governed by the brine volume fraction (Culha et al., 2020). Constraints on properties of the ice shell will be necessary to robustly constrain the properties of the sub-ice ocean, which represents an important goal in assessing Europa's habitability. Beyond Europa, missions to other potential ocean worlds such as Enceladus, Titan, Ganymede, and Triton could benefit from this approach, particularly at the science requirements development stage. Future work incorporating the presence of low eutectic surface species (e.g., sulfuric acid, perchlorates) in the framework presented here represents an avenue for understanding how liquid water in the ice shell might serve as a signature of surface-ice-ocean exchange and ultimately Europa's potential habitability.

Open Research

The code base used to model the volume fraction of brine and salt in ice for this work is preserved at https://doi.org/10.5281/zenodo.6813344 and licensed under the GNU General Public License v3.0.

Acknowledgments

NSW was supported by the G. Unger Vetlesen Foundation. MGF was supported by the Research England Expanding Excellence in England (E3) fund (grant code 124.18). KMS was supported by the NASA Network for Life Detection project Oceans Across Space and Time (Grant Number: 80NSSC18K1301). DDB was supported by the G. Unger Vetlesen Foundation.

References

Assur, A. (1960). *Composition of sea ice and its tensile strength* (Vol. 44). US Army Snow, Ice and Permafrost Research Establishment.

Barr, A. C., & McKinnon, W. B. (2007). Convection in ice i shells and mantles with self-consistent grain size. *Journal of Geophysical Research: Planets*, *112*(E2).

Blankenship, D. D., Ray, T., Plaut, J., Moussessian, A., Patterson, W., Romero-Wolf, A., ... others (2018). Reason for europa. *42nd COSPAR Scientific Assembly*, *42*, B5–3.

Blankenship, D. D., Young, D. A., Moore, W. B., & Moore, J. C. (2009). Radar sounding of europa's subsurface properties and processes: The view from earth. *Europa*, 631–654.

Bode, A. A., Pulles, P. G., Lutz, M., Poulisse, W. J., Jiang, S., Meijer, J. A., ... Vlieg, E. (2015). Sodium chloride dihydrate crystals: morphology, nucleation, growth, and inhibition. *Crystal Growth & Design*, *15*(7), 3166–3174.

Brown, M. E. (2001). Potassium in europa's atmosphere. *Icarus*, *151*(2), 190–195.

Brown, M. E., & Hand, K. (2013). Salts and radiation products on the surface of europa. *The Astronomical Journal*, *145*(4), 110.

Bruzzone, L., Plaut, J. J., Alberti, G., Blankenship, D. D., Bovolo, F., Campbell, B. A., ... others (2013). Rime: Radar for icy moon exploration. In *2013 ieee international geoscience and remote sensing symposium-igarss* (pp. 3907–3910).

Buffo, J., Meyer, C., & Parkinson, J. (2021). Dynamics of a solidifying icy satellite shell. *Journal of Geophysical Research: Planets*, e2020JE006741.

Buffo, J., Schmidt, B., & Huber, C. (2018). Multiphase reactive transport and platelet ice accretion in the sea ice of mcmurdo sound, antarctica. *Journal of Geophysical Research: Oceans*, *123*(1), 324–345.

Buffo, J., Schmidt, B. E., Huber, C., & Walker, C. C. (2020). Entrainment and dynamics of ocean-derived impurities within europa's ice shell. *Journal of Geophysical Research: Planets*, *125*(10), e2020JE006394.

Butler, B. M. (2016). *Mineral dynamics in sea ice brines* (PhD Thesis). Prifysgol Bangor University.

Butler, B. M., & Kennedy, H. (2015). An investigation of mineral dynamics in frozen seawater brines by direct measurement with synchrotron x-ray powder diffraction. *Journal of Geophysical Research: Oceans*, *120*(8), 5686–5697.

Butler, B. M., Papadimitriou, S., Day, S. J., & Kennedy, H. (2017). Gypsum and hydrohalite dynamics in sea ice brines. *Geochimica et Cosmochimica Acta*, *213*,

17–34.

Butler, B. M., Papadimitriou, S., & Kennedy, H. (2016). The effect of mirabilite precipitation on the absolute and practical salinities of sea ice brines. *Marine Chemistry*, *184*, 21–31.

Butler, B. M., Papadimitriou, S., Santoro, A., & Kennedy, H. (2016). Mirabilite solubility in equilibrium sea ice brines. *Geochimica et Cosmochimica Acta*, *182*, 40–54.

Carlson, R., Calvin, W., Dalton, J., Hansen, G., Hudson, R., Johnson, R., ... Moore, M. (2009). Europa's surface composition. *Europa*, *283*.

Chang, B., Consiglio, A. N., Lilley, D., Prasher, R., Rubinsky, B., Journaux, B., & Powell-Palm, M. J. (2022). On the pressure dependence of salty aqueous eutectics. *Cell Reports Physical Science*, 100856.

Chivers, C., Buffo, J., & Schmidt, B. (2021). Thermal and chemical evolution of small, shallow water bodies in europa's ice shell. *Journal of Geophysical Research: Planets*, *126*(5), e2020JE006692.

Cox, G. F., & Weeks, W. F. (1983). Equations for determining the gas and brine volumes in sea-ice samples. *Journal of Glaciology*, *29*(102), 306–316.

Culha, C., Schroeder, D. M., Jordan, T. M., & Haynes, M. S. (2020). Assessing the detectability of europa's eutectic zone using radar sounding. *Icarus*, *339*, 113578.

Deschamps, F., & Sotin, C. (2001). Thermal convection in the outer shell of large icy satellites. *Journal of Geophysical Research: Planets*, *106*(E3), 5107–5121.

Des Marais, D. J., Nuth III, J. A., Allamandola, L. J., Boss, A. P., Farmer, J. D., Hoehler, T. M., ... others (2008). The nasa astrobiology roadmap. *Astrobiology*, *8*(4), 715–730.

Drebushchak, V., Drebushchak, T., Ogienko, A., & Yunoshev, A. (2019). Crystallization of sodium chloride dihydrate (hydrohalite). *Journal of Crystal Growth*, *517*, 17–23.

Drebushchak, V., Ogienko, A., & Yunoshev, A. (2017). Metastable eutectic melting in the nacl-h2o system. *Thermochimica acta*, *647*, 94–100.

Elsenousy, A., Hanley, J., & Chevrier, V. F. (2015). Effect of evaporation and freezing on the salt paragenesis and habitability of brines at the phoenix landing site. *Earth and Planetary Science Letters*, *421*, 39–46.

Feistel, R. (2008). A gibbs function for seawater thermodynamics for- 6 to 80 c and salinity up to 120 g kg–1. *Deep Sea Research Part I: Oceanographic Research Papers*, *55*(12), 1639–1671.

Feistel, R., & Wagner, W. (2006). A new equation of state for h 2 o ice ih. *Journal of Physical and Chemical Reference Data*, *35*(2), 1021–1047.

Fischer, P. D., Brown, M. E., & Hand, K. (2015). Spatially resolved spectroscopy of europa: The distinct spectrum of large-scale chaos. *The Astronomical Journal*, *150*(5), 164.

Fortes, A., Wood, I., & Knight, K. (2008). The crystal structure and thermal expansion tensor of mgso4–11d2o (meridianiite) determined by neutron powder diffraction. *Physics and Chemistry of Minerals*, *35*(4), 207–221.

Fox-Powell, M. G., & Cousins, C. R. (2021). Partitioning of crystalline and amorphous phases during freezing of simulated enceladus ocean fluids. *Journal of Geophysical Research: Planets*, *126*(1), e2020JE006628.

Geilfus, N.-X., Galley, R., Cooper, M., Halden, N., Hare, A., Wang, F., ... Rysgaard, S. (2013). Gypsum crystals observed in experimental and natural sea ice. *Geophysical research letters*, *40*(24), 6362–6367.

Genceli, F. E., Lutz, M., Spek, A. L., & Witkamp, G.-J. (2007). Crystallization and characterization of a new magnesium sulfate hydrate mgso4· 11h2o. *Crystal Growth and Design*, *7*(12), 2460–2466.

Gitterman, K. (1937). Thermal analysis of seawater. *CRREL TL*, *287*.

Golden, K., Ackley, S., & Lytle, V. (1998). The percolation phase transition in sea ice. *Science*, *282*(5397), 2238–2241.

Golden, K., Eicken, H., Heaton, A., Miner, J., Pringle, D., & Zhu, J. (2007). Thermal evolution of permeability and microstructure in sea ice. *Geophysical research letters*, *34*(16).

Grasset, O., Dougherty, M., Coustenis, A., Bunce, E., Erd, C., Titov, D., ... others (2013). Jupiter icy moons explorer (juice): An esa mission to orbit ganymede and to characterise the jupiter system. *Planetary and Space Science*, *78*, 1–21.

Hand, K., Sotin, C., Hayes, A., & Coustenis, A. (2020). On the habitability and future exploration of ocean worlds. *Space Science Reviews*, *216*(5), 1–24.

Hendrix, A. R., Cassidy, T. A., Johnson, R. E., Paranicas, C., & Carlson, R. W. (2011). Europa's disk-resolved ultraviolet spectra: Relationships with plasma

flux and surface terrains. *Icarus*, *212*(2), 736–743.

Hibbitts, C., Stockstill-Cahill, K., Wing, B., & Paranicas, C. (2019). Color centers in salts-evidence for the presence of sulfates on europa. *Icarus*, *326*, 37–47.

Hörst, S., & Brown, M. E. (2013). A search for magnesium in europa's atmosphere. *The Astrophysical Journal Letters*, *764*(2), L28.

Howell, S. M. (2021). The likely thickness of europa's icy shell. *The Planetary Science Journal*, *2*(4), 129.

Howell, S. M., & Pappalardo, R. T. (2020). Nasa's europa clipper—a mission to a potentially habitable ocean world. *Nature communications*, *11*(1), 1–4.

Hussmann, H., & Spohn, T. (2004). Thermal-orbital evolution of io and europa. *Icarus*, *171*(2), 391–410.

Kalousová, K., Schroeder, D. M., & Soderlund, K. M. (2017). Radar attenuation in europa's ice shell: Obstacles and opportunities for constraining the shell thickness and its thermal structure. *Journal of Geophysical Research: Planets*, *122*(3), 524–545.

Kargel, J. S., Kaye, J. Z., Head III, J. W., Marion, G. M., Sassen, R., Crowley, J. K., ... Hogenboom, D. L. (2000). Europa's crust and ocean: origin, composition, and the prospects for life. *Icarus*, *148*(1), 226–265.

Leppäranta, M., & Manninen, T. (1988). The brine and gas content of sea ice with attention to low salinities and high temperatures.

Light, B., Brandt, R. E., & Warren, S. G. (2009). Hydrohalite in cold sea ice: Laboratory observations of single crystals, surface accumulations, and migration rates under a temperature gradient, with application to "snowball earth". *Journal of Geophysical Research: Oceans*, *114*(C7).

Ligier, N., Poulet, F., Carter, J., Brunetto, R., & Gourgeot, F. (2016). Vlt/sinfoni observations of europa: new insights into the surface composition. *The Astronomical Journal*, *151*(6), 163.

Marion, G., Catling, D., Kargel, J., & Crowley, J. (2016). Modeling calcium sulfate chemistries with applications to mars. *Icarus*, *278*, 31–37.

Marion, G., Farren, R., & Komrowski, A. (1999). Alternative pathways for seawater freezing. *Cold Regions Science and Technology*, *29*(3), 259–266.

Marion, G., Fritsen, C. H., Eicken, H., & Payne, M. C. (2003). The search for life on europa: limiting environmental factors, potential habitats, and earth

analogues. *Astrobiology*, *3*(4), 785–811.

Marion, G., Kargel, J., Catling, D., & Lunine, J. (2012). Modeling ammonia–ammonium aqueous chemistries in the solar system's icy bodies. *Icarus*, *220*(2), 932–946.

Marion, G., Kargel, J., Catling, D., & Lunine, J. (2014). Modeling nitrogen-gas,-liquid,-solid chemistries at low temperatures (173–298 k) with applications to titan. *Icarus*, *236*, 1–8.

Marion, G., Kargel, J., Crowley, J., & Catling, D. (2013). Sulfite–sulfide–sulfate–carbonate equilibria with applications to mars. *Icarus*, *225*(1), 342–351.

Marion, G., Kargel, J., & Tan, S. (2015). Modeling nitrogen and methane with ethane and propane gas hydrates at low temperatures (173–290 k) with applications to titan. *Icarus*, *257*, 355–361.

Marion, G., & Kargel, J. S. (2007). *Cold aqueous planetary geochemistry with frezchem: From modeling to the search for life at the limits*. Springer Science & Business Media.

Marion, G., Kargel, J. S., Catling, D. C., & Jakubowski, S. D. (2005). Effects of pressure on aqueous chemical equilibria at subzero temperatures with applications to europa. *Geochimica et Cosmochimica Acta*, *69*(2), 259–274.

Marion, G., Millero, F., & Feistel, R. (2009). Precipitation of solid phase calcium carbonates and their effect on application of seawater s a–t–p models. *Ocean Science*, *5*(3), 285–291.

Maus, S. (2020). The plate spacing of sea ice. *Annals of Glaciology*, *61*(83), 408–425.

Maus, S., Schneebeli, M., & Wiegmann, A. (2021). An x-ray micro-tomographic study of the pore space, permeability and percolation threshold of young sea ice. *The Cryosphere*, *15*(8), 4047–4072.

McCord, T. B., Hansen, G. B., Fanale, F., Carlson, R., Matson, D., Johnson, T., ... others (1998). Salts on europa's surface detected by galileo's near infrared mapping spectrometer. *Science*, *280*(5367), 1242–1245.

McKinnon, W. B. (1999). Convective instability in europa's floating ice shell. *Geophysical Research Letters*, *26*(7), 951–954.

Millero, F. J., Feistel, R., Wright, D. G., & McDougall, T. J. (2008). The composition of standard seawater and the definition of the reference-composition

salinity scale. *Deep Sea Research Part I: Oceanographic Research Papers*, *55*(1), 50–72.

Mitri, G., & Showman, A. P. (2005). Convective–conductive transitions and sensitivity of a convecting ice shell to perturbations in heat flux and tidal-heating rate: Implications for europa. *Icarus*, *177*(2), 447–460.

Nelson, K. H., & Thompson, T. G. (1954). Deposition of salts from sea water by frigid concentration.

Ojakangas, G. W., & Stevenson, D. J. (1989). Thermal state of an ice shell on europa. *Icarus*, *81*(2), 220–241.

Parkhurst, D. L., Appelo, C., et al. (2013). Description of input and examples for phreeqc version 3—a computer program for speciation, batch-reaction, one-dimensional transport, and inverse geochemical calculations. *US geological survey techniques and methods*, *6*(A43), 497.

Petrich, C., & Eicken, H. (2017). Overview of sea ice growth and properties. *Sea ice*, 1–41.

Petrich, C., Langhorne, P., & Eicken, H. (2011). Modelled bulk salinity of growing first-year sea ice and implications for ice properties in spring. In *Proceedings of the international conference on port and ocean engineering under arctic conditions.*

Petrich, C., Langhorne, P. J., & Sun, Z. F. (2006). Modelling the interrelationships between permeability, effective porosity and total porosity in sea ice. *Cold Regions Science and Technology*, *44*(2), 131–144.

Pitzer, K. S. (1991). Ion interaction approach: theory and data correlation. *Activity coefficients in electrolyte solutions*, *2*, 75–153.

Postberg, F., Schmidt, J., Hillier, J., Kempf, S., & Srama, R. (2011). A salt-water reservoir as the source of a compositionally stratified plume on enceladus. *Nature*, *474*(7353), 620–622.

Pringle, D., Miner, J., Eicken, H., & Golden, K. (2009). Pore space percolation in sea ice single crystals. *Journal of Geophysical Research: Oceans*, *114*(C12).

Ringer, W. (1906). De varanderingon in samenstelling van zeewater bij het bevriezen. *Chemisch Weekblad*, *3*(15), 223–249.

Ruiz, J., Montoya, L., López, V., & Amils, R. (2007). Thermal diapirism and the habitability of the icy shellof europa. *Origins of Life and Evolution of Bio-*

spheres, *37*(3), 287–295.

Shematovich, V. (2018). Ocean worlds in the outer regions of the solar system. *Solar System Research*, *52*(5), 371–381.

Soderlund, K. M., Kalousová, K., Buffo, J. J., Glein, C. R., Goodman, J. C., Mitri, G., ... others (2020). Ice-ocean exchange processes in the jovian and saturnian satellites. *Space Science Reviews*, *216*(5), 1–57.

Squyres, S. W., Reynolds, R. T., Cassen, P. M., & Peale, S. J. (1983). Liquid water and active resurfacing on europa. *Nature*, *301*(5897), 225–226.

Steinbrügge, G., Voigt, J. R., Wolfenbarger, N. S., Hamilton, C., Soderlund, K., Young, D., ... Schroeder, D. M. (2020). Brine migration and impact-induced cryovolcanism on europa. *Geophysical Research Letters*, *47*(21), e2020GL090797.

Tan, S., Sekine, Y., & Kuzuhara, M. (2022). Aspatially resolved observations of europa's surface with subaru/ircs at 1.0–1.8 μm: Upper limits to the abundances of hydrated cl-bearing salts. *The Planetary Science Journal*, *3*(3), 70.

Tobie, G., Choblet, G., & Sotin, C. (2003). Tidally heated convection: Constraints on europa's ice shell thickness. *Journal of Geophysical Research: Planets*, *108*(E11).

Toner, J., & Catling, D. (2017a). A low-temperature aqueous thermodynamic model for the na–k–ca–mg–cl–so4 system incorporating new experimental heat capacities in na2so4, k2so4, and mgso4 solutions. *Journal of Chemical & Engineering Data*, *62*(10), 3151–3168.

Toner, J., Catling, D., & Light, B. (2014a). The formation of supercooled brines, viscous liquids, and low-temperature perchlorate glasses in aqueous solutions relevant to mars. *Icarus*, *233*, 36–47.

Toner, J., Catling, D., & Light, B. (2014b). Soluble salts at the phoenix lander site, mars: A reanalysis of the wet chemistry laboratory data. *Geochimica et Cosmochimica Acta*, *136*, 142–168.

Toner, J., Catling, D., & Light, B. (2015). A revised pitzer model for low-temperature soluble salt assemblages at the phoenix site, mars. *Geochimica et Cosmochimica Acta*, *166*, 327–343.

Toner, J., & Catling, D. C. (2017b). A low-temperature thermodynamic model for the na-k-ca-mg-cl system incorporating new experimental heat capacities

in kcl, mgcl2, and cacl2 solutions. *Journal of Chemical & Engineering Data*, *62*(3), 995–1010.

Trumbo, S. K., Brown, M. E., & Hand, K. (2019). Sodium chloride on the surface of europa. *Science advances*, *5*(6), eaaw7123.

Turner, A. K., Hunke, E. C., & Bitz, C. M. (2013). Two modes of sea-ice gravity drainage: A parameterization for large-scale modeling. *Journal of Geophysical Research: Oceans*, *118*(5), 2279–2294.

Vance, S. D., Barge, L. M., Cardoso, S. S., & Cartwright, J. H. (2019). Self-assembling ice membranes on europa: Brinicle properties, field examples, and possible energetic systems in icy ocean worlds. *Astrobiology*, *19*(5), 685–695.

Vancoppenolle, M., Madec, G., Thomas, M., & McDougall, T. J. (2019). Thermodynamics of sea ice phase composition revisited. *Journal of Geophysical Research: Oceans*, *124*(1), 615–634.

Vilella, K., Choblet, G., Tsao, W.-E., & Deschamps, F. (2020). Tidally heated convection and the occurrence of melting in icy satellites: Application to europa. *Journal of Geophysical Research: Planets*, *125*(3), e2019JE006248.

Wolfenbarger, N. S. (2022). Brinevolumefraction. (Initial Release). Retrieved from `http://doi.org/10.5281/ZENODO.6813344`

Wolfenbarger, N. S., Buffo, J. J., Soderlund, K. M., & Blankenship, D. D. (2022). Ice shell structure and composition of ocean worlds: Insights from accreted ice on earth. *Astrobiology*, *22*(8).

Zolotov, M. Y. (2007). An oceanic composition on early and today's enceladus. *Geophysical Research Letters*, *34*(23).

Zolotov, M. Y., & Shock, E. L. (2001). Composition and stability of salts on the surface of europa and their oceanic origin. *Journal of Geophysical Research: Planets*, *106*(E12), 32815–32827.

Zubov, N. N. (1945). *L'dy arktiki*. Izdatel'stvo glavsevmorputi.

Supporting Information for "Compositional Controls on the Distribution of Brine in Europa's Ice Shell"

N. S. Wolfenbarger[1], M. G. Fox-Powell[2], J. J. Buffo[3], K. M. Soderlund[1], D. D. Blankenship[1]

[1]Institute for Geophysics, Jackson School of Geosciences, University of Texas at Austin, Austin, Texas, USA

[2]AstrobiologyOU, The Open University, Walton Hall, Milton Keynes, UK

[3]Dartmouth College, Hanover, New Hampshire, USA

Contents of this file

Introduction This supporting information includes derivations, figures, and tables that provide important background and context for the published manuscript. Derivations 1.1 – 1.3 represent equations which are incorporated into the code base used to obtain the results published in the main text. The derivations presented here illustrate: (1.1) how to obtain our expression for brine volume fraction from the work of Cox and Weeks (1983), (1.2) how the density of solid salts is calculated from the output of FREZCHEM, and (1.3) how the solid salt volume fraction is estimated for temperatures below the eutectic. Figures S1 and S2 demonstrate the sensitivity of the phase behavior functions

to the ocean salinity specified in the FREZCHEM v15.1 input file for our analog endmember ocean compositions. Figure S3 is a reproduction of the bottom row of Fig. 8 where only brine volume fraction is shown. Table S1 presents the temperature at which each salt mineral starts to precipitate in the FREZCHEM v13.3 simulations of terrestrial seawater shown in Fig. 2. Tables S2 – S5 provide the best fit coefficients for the phase behavior functions used to estimate brine volume fraction for terrestrial seawater, our binary endmember compositions, and our analog endmember compositions, respectively. Table S6 presents the temperature at which each salt mineral starts to precipitate in the FREZCHEM v15.1 simulations of our analog endmember compositions shown in Fig. S1 and S2. Table S7 presents a comparison of salt precipitation sequences from PHREEQC (using the ColdChem and frezchem databases) and FREZCHEM (v13.3 and v15.1).

1. Derivations

1.1. Brine Volume Fraction, $\frac{V_b}{V}(T)$

Cox and Weeks (1983) derive an expression (Eq. 5 in Cox and Weeks (1983)) for the brine volume fraction of sea ice as a function of temperature, T, given by

$$\frac{V_b}{V}(T) = \frac{\rho S}{F_1(T)} \tag{1}$$

where ρ is the bulk density of sea ice in units of g/cm^3 and S is the bulk ice salinity in ppt. Their expression for the sea ice bulk density (Eq. 15 in Cox and Weeks (1983)) is given by

$$\rho = \left(1 - \frac{V_a}{V}\right) \frac{\rho_i F_1(T)}{F_1(T) - \rho_i S F_2(T)} \tag{2}$$

where ρ_i is the pure ice density in units of g/cm^3 and $F_1(T)$ and $F_2(T)$ are the phase behavior functions. If we substitute Eq. (2) into Eq. (1) we obtain

$$\frac{V_b}{V}(T) = \left(1 - \frac{V_a}{V}\right) \frac{\rho_i S}{F_1(T) - \rho_i S F_2(T)} \tag{3}$$

which is equivalent to the form of the brine volume equation provided as (1.8) in Petrich and Eicken (2017).

1.2. Density of Solid Salts, $\rho_{ss}(T)$

The density of solid salts at a given temperature is given by

$$\rho_{ss}(T) = \frac{m_{ss}(T)}{V_{ss}(T)} \tag{4}$$

where $m_{ss}(T)$ is the total mass of solid salts present and $V_{ss}(T)$ is the total volume of solid salts present at the same temperature. The total mass of solid salts can be expressed as

$$m_{ss}(T) = \sum_{n=1}^{N} m_{ss,n}(T) \tag{5}$$

where $m_{ss,n}(T)$ represents the total mass of the nth solid salt of N solid salts present at a given temperature. This quantity can be calculated from the "Moles" column of the "Solid SPECIES" section in FREZCHEM output file or "Final Moles in assemblage" column of the PHREEQC output file. The total volume of solid salts can be similarly expressed as

$$V_{ss}(T) = \sum_{n=1}^{N} V_{ss,n}(T) \tag{6}$$

where $V_{ss,n}(T)$ represents the total volume of the nth solid salt present at a given temperature. $V_{ss,n}(T)$ can be equivalently expressed as

$$V_{ss}(T) = \sum_{n=1}^{N} \frac{m_{ss,n}(T)}{\rho_{ss,n}} \tag{7}$$

where $\rho_{ss,n}$ represents the density of the nth solid salt, assumed to be temperature invariant. Although $\rho_{ss,n}$ cannot be obtained from the FREZCHEM output file, we adopt the molar volumes specified in the relevant documentation (Marion et al., 2005, 2012). Molar volumes can also be found in the frezchem database file in PHREEQC, although we note that they are not present in the ColdChem database file. The total density of solids salts can thus be expressed as

$$\rho_{ss}(T) = \frac{\sum_{n=1}^{N} m_{ss,n}}{\sum_{n=1}^{N} \frac{m_{ss,n}}{\rho_{ss,n}}}. \tag{8}$$

1.3. Solid Salt Volume Fraction Below the Eutectic, $\frac{V_{ss}}{V}(T \leq T_{eut})$

The solid salt volume fraction below the eutectic temperature is governed by the total mass fraction of solid salts that forms once the solution solidifies completely and the density of the solid salt and ice phases. We can express this as

$$\frac{V_{ss}}{V}(T \leq T_{eut}) = \frac{x_{ss}(T = T_{eut})}{x_{ss}(T = T_{eut}) + (1 - x_{ss}(T = T_{eut}))\frac{\rho_{ss}(T=T_{eut})}{\rho_i(T)}} \tag{9}$$

where $x_{ss}(T = T_{eut})$ represents the total mass fraction of solid salts which precipitate at/beyond the eutectic and $\rho_{ss}(T = T_{eut})$ represents the total salt density at/beyond the eutectic. Although in this work we define the eutectic temperature as the last convergent temperature step, because brine is remaining at this temperature step, additionally salt precipitation occurs below this temperature up through the "true" eutectic. Note that although FREZCHEM specifies which minerals are precipitating at/beyond the eutectic, it does not calculate the amount of each mineral precipitating[1]. As such, we must estimate the mass of solid salts precipitating beyond the final temperature step. To do this, we define a linear system

$$\mathbf{d} = \mathbf{C}\mathbf{x} + \epsilon \tag{10}$$

where $\mathbf{d}$ is a column vector containing the moles of ionic species present at the final convergent temperature step, $\mathbf{C}$ is a matrix which maps the ionic species present at the final convergent temperature step to the solid salts precipitating beyond the final convergent temperature, and $\mathbf{x}$ represents the number of moles of each solid species which forms beyond the final convergent temperature. We want to find $\mathbf{x}$ such that concentration of dissolved ions remaining beyond the eutectic, ϵ, is minimized. Because we are only allowing for precipitation beyond the final temperature step (and not dissolution), we must also impose the constraint that $\mathbf{x}$ is greater than

zero. Therefore, the solution to this problem is obtained via constrained least squares (`lsqlin` in MATLAB). For both of the analog endmember compositions assumed in this work, the linear system is represented by

$$\mathbf{d} = \begin{bmatrix} [\mathrm{Cl}^-] \\ [\mathrm{Mg}^{2+}] \\ [\mathrm{Na}^-] \\ [\mathrm{SO}_4^{2-}] \end{bmatrix} \tag{11}$$

$$\mathbf{x} = \begin{bmatrix} [\mathrm{NaCl} \cdot 2\mathrm{H_2O}] \\ [\mathrm{Na_2SO_4} \cdot 10\mathrm{H_2O}] \\ [\mathrm{MgSO_4} \cdot 11\mathrm{H_2O}] \end{bmatrix} \tag{12}$$

$$\mathbf{C} = \begin{bmatrix} 1 & 0 & 0 \\ 0 & 0 & 1 \\ 1 & 2 & 0 \\ 0 & 1 & 1 \end{bmatrix} \tag{13}$$

subject to the constraint $\mathbf{Ax} \leq \mathbf{b}$, where $\mathbf{A}= -I$ and $\mathbf{b}= \vec{0}$. We can obtain $m_{ss}(T \leq T_{eut})$ by summing the mass obtained from solving the constrained least squares problem above, $m_{ss}(T = T_{eut})$, to the cumulative mass present at the eutectic temperature, $m_{ss}(T > T_{eut})$. This can be expressed by the following:

$$m_{ss}(T \leq T_{eut}) = m_{ss}(T > T_{eut}) + m_{ss}(T = T_{eut}). \tag{14}$$

However, this specifically represents the mass of solid salts for the initial brine salinity specified in the FREZCHEM (or PHREEQC) input file. We need to scale this mass for a bulk ice salinity of interest, S. This can be done by multiplying $m_{ss}(T \leq T_{eut})$ by the ratio of the mass of salt in a system of bulk salinity S, defined as $m_s^b(T = T_0, S)$, to the mass of salt used to derive $m_{ss}(T \leq T_{eut})$ (i.e., the mass of salt specified in the input file, defined as $m_s^b(T = T_0)$). This yields an expression for the mass fraction of solid salts at the eutectic of

$$x_{ss}(T = T_{eut}) = \left(\frac{m_s^b(T = T_0, S)}{m_s^b(T = T_0)}\right)\left(\frac{m_{ss}(T \leq T_{eut})}{M + m_s^b(T = T_0, S)}\right) \tag{15}$$

where $m_s^b(T = T_0, S)$ is given by

$$m_s^b(T = T_0, S) = \frac{1000S}{1000 - S} \tag{16}$$

which represents a conversion of the bulk ice salinity, S from units of grams of salt per kg solution (ppt) to grams of salt per kg of water. Substituting Eq. (16) into Eq. (15) yields

$$x_{ss}(T = T_{eut}) = \left(\frac{\frac{1000S}{1000-S}}{m_s^b(T = T_0)}\right)\left(\frac{m_{ss}(T \leq T_{eut})}{M + \frac{1000S}{1000-S}}\right) \tag{17}$$

where M is the total mass of water (always 1000 g in our simulations). Taking $M = 1000$ g, this simplifies to

$$x_{ss}(T = T_{eut}) = \frac{Sm_{ss}(T \leq T_{eut})}{1000m_s^b(T = T_0)} \tag{18}$$

We define a scale factor, k^*, as

$$k^* = \frac{m_{ss}(T \leq T_{eut})}{m_s^b(T = T_0)} \tag{19}$$

which effectively represents the increase in the mass of solid salts at/beyond the eutectic relative to the initial mass of dissolved salts, resulting from the hydration of salts as the solution freezes. Substituting Eq. (18) and Eq. (19) into Eq. (9) yields

$$\frac{V_{ss}}{V}(T \leq T_{eut}) = \frac{Sk^*}{Sk^* + (1000 - Sk^*)\frac{\rho_{ss}(T=T_{eut})}{\rho_i(T)}}. \tag{20}$$

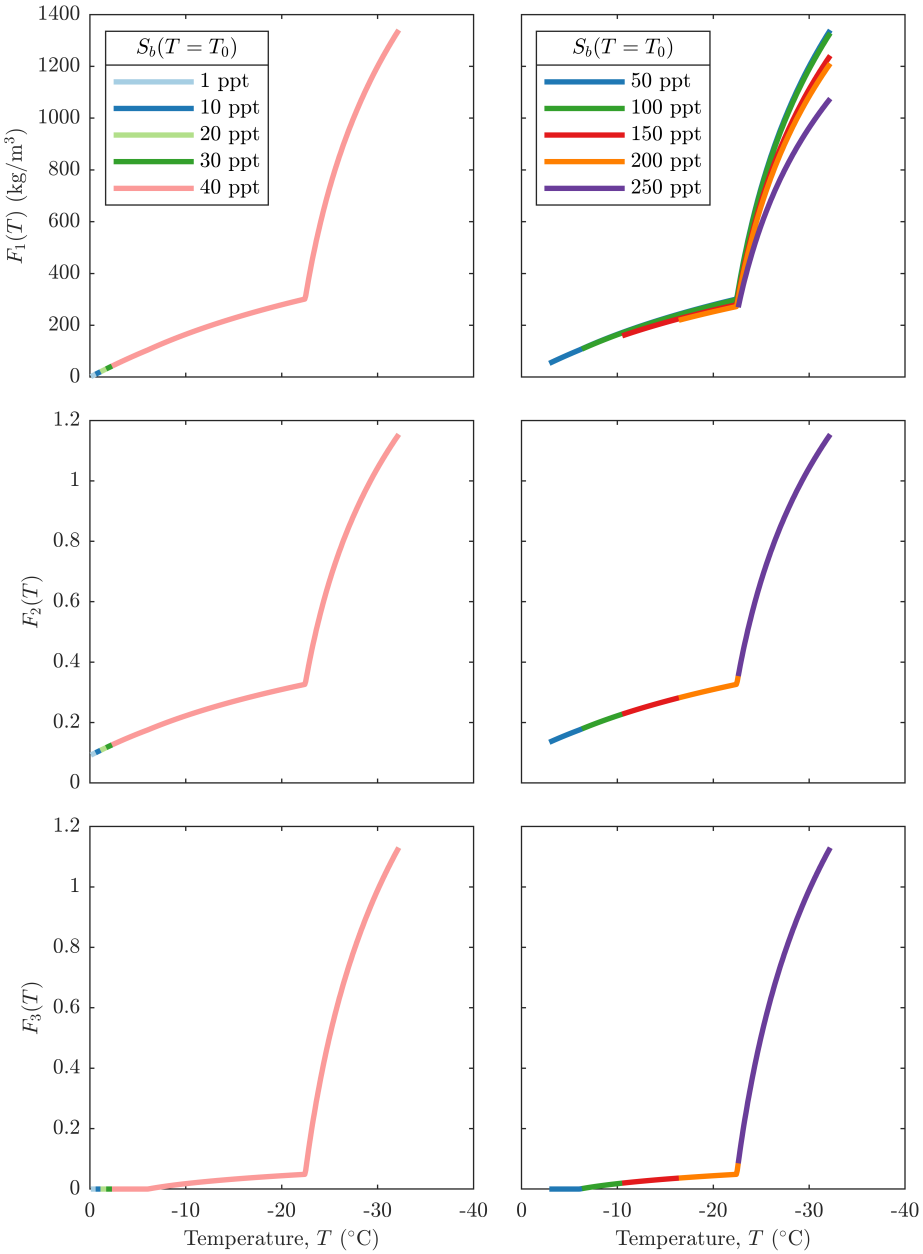

Figure S1. Phase behavior functions derived from FREZCHEM simulations of our Cl-dominated Europan ocean, assuming a range of ocean salinities $S_b(T = T_0)$.

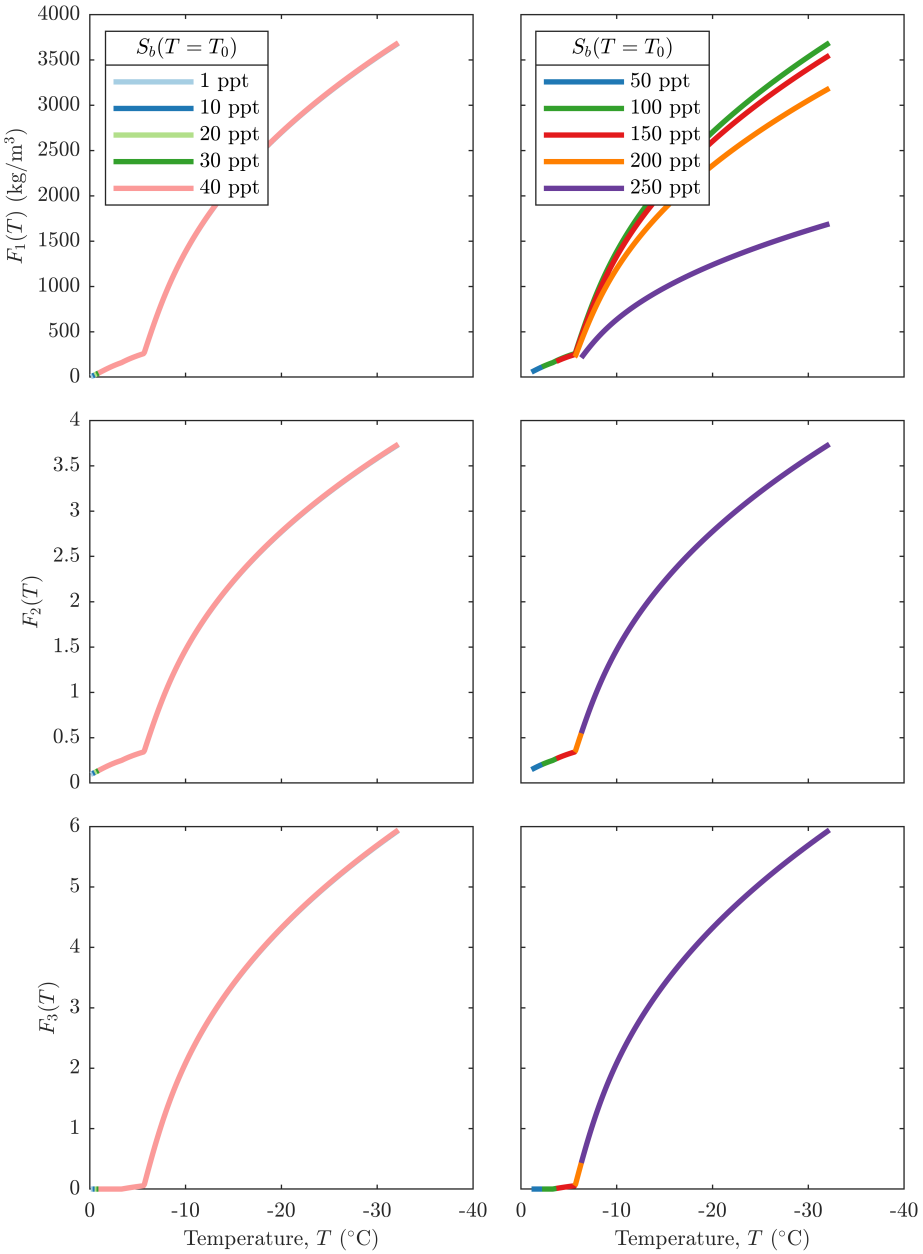

Figure S2. Phase behavior functions derived from FREZCHEM simulations of our SO_4-dominated Europan ocean, assuming a range of ocean salinities $S_b(T = T_0)$.

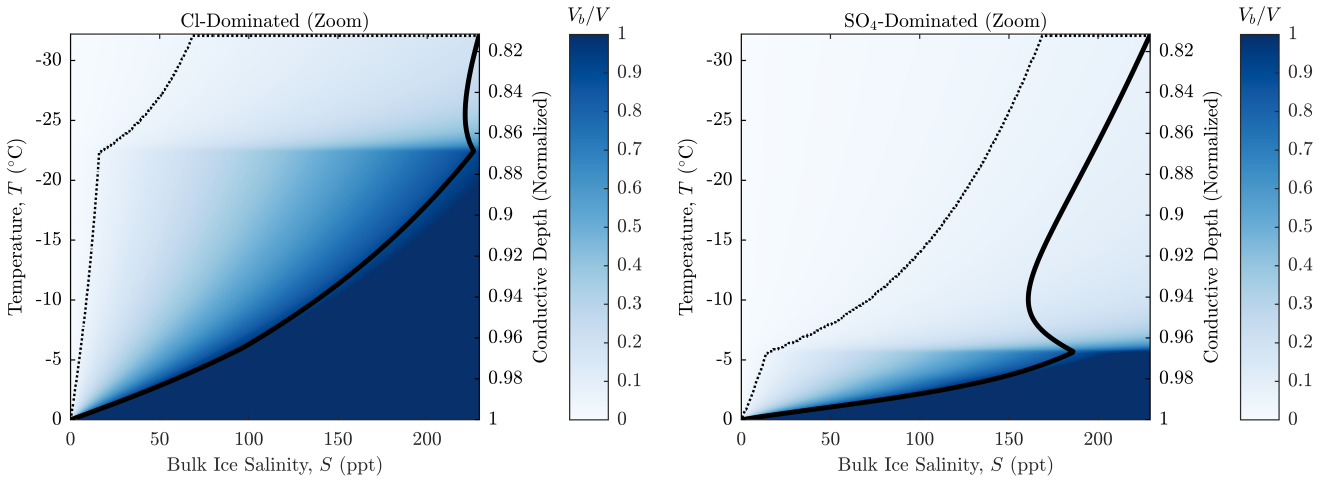

Figure S3. Brine volume fraction for the bottom $\sim 20\%$ of a conductive ice layer at Europa assuming analog endmember compositions for the ocean and a fixed pressure of 1 atm. The vertical axis corresponds to the temperature at a given depth within the ice shell. The thick solid curve represents the brine salinity as a function of temperature, whereas the thin dotted curve corresponds to a brine volume fraction of 0.05.

Table S1. The temperature at which a specified salt starts precipitating for terrestrial seawater of salinity, $S_b(T = T_0)$ at a pressure of 1 atm, predicted by FREZCHEM v13.3. Note that for a seawater salinity greater than 100 ppt certain salts begin precipitating at higher temperatures, influencing the phase behavior functions shown in Fig. 2.

$S_b(T = T_0)$ (ppt)	1	10	20	30	40	50	100	150	200	250
	Temperature, T (°C)									
Ikaite										
$CaCO_3{\cdot}6H_2O$	−4.9	−4.9	−4.9	−4.9	−4.9	−4.9	≥0.0	≥0.0	≥0.0	≥0.0
Gypsum										
$CaSO_4{\cdot}2H_2O$	−6.2	−6.2	−6.2	−6.2	−6.2	−6.2	−6.2	≥0.0	≥0.0	≥0.0
Mirabilite										
$Na_2SO_4{\cdot}10H_2O$	−6.4	−6.4	−6.4	−6.4	−6.4	−6.4	−6.4	−3.4	−1.0	≥0.0
Hydrohalite										
$NaCl{\cdot}2H_2O$	−22.9	−22.9	−22.9	−22.9	−22.9	−22.9	−22.9	−22.9	−22.9	−22.9
NaBr	−22.9	−22.9	−22.9	−22.9	−22.9	−22.9	−22.9	−22.9	−22.9	−22.9
Meridianiite										
$MgSO_4{\cdot}11H_2O$	−33.3	−33.3	−33.3	−33.3	−33.3	−33.3	−33.3	−33.3	−33.3	−33.3
Sylvite										
KCl	−33.4	−33.4	−33.4	−33.4	−33.4	−33.4	−33.4	−33.4	−33.4	−33.4
$MgCl_2{\cdot}12H_2O$[a]	-	-	-	-	-	-	-	-	-	-

[a]Our version of FREZCHEM v13.3 fails to display text that $MgCl_2{\cdot}12H_2O$ is precipitating at/beyond the eutectic, possibly due to a compiler issue; however this is known from previous works (Marion et al., 1999; Vancoppenolle et al., 2019). We also note that this text appears to be absent in the FREZCHEM v13.3 output files of some other authors (see Vancoppenolle et al. (2019)).

Table S2. Phase behavior functions for seawater (Marion et al., 2009) derived from a best fit to the output of FREZCHEM v13.3. The piecewise polynomial functions were optimized to ensure that they were continuous across the temperature domain from 0 °C to −33 °C and that $F_1(0) = 0$ and $F_2(0) = \frac{\rho_w(T=T_m)}{\rho_i(T=T_m)} - 1$. The temperature breakpoints precede major precipitation events that occur along the freezing pathway (i.e., the formation of hydrohalite at −22.9 °C and meridianiite at −33.3 °C). F_3 is zero above −6.4 °C, where mirabilite begins to form, since a negligible amount of salt precipitates above this temperature. Brine is no longer stable below the eutectic temperature of −36.2 °C.

$F_1(T) = a_1T^3 + b_1T^2 + c_1T + d_1$				
Temperature (°C)	a_1	b_1	c_1	d_1
$0 \geq T \geq -22.8$	-1.2639×10^{-3}	-2.8711×10^{-1}	-1.9451×10^{1}	0
$-22.8 \geq T \geq -33.3$	-4.3760×10^{-1}	-4.2299×10^{1}	-1.4294×10^{3}	-1.5479×10^{4}
$-33.3 > T \geq -36.2$	-2.1724×10^{-1}	-2.6462×10^{1}	-1.1510×10^{3}	-1.4946×10^{4}
$F_2(T) = a_2T^3 + b_2T^2 + c_2T + d_2$				
Temperature (°C)	a_2	b_2	c_2	d_2
$0 \geq T \geq -22.8$	-3.2209×10^{-6}	-3.1992×10^{-4}	-1.6257×10^{-2}	9.0673×10^{-2}
$-22.8 \geq T \geq -33.3$	-3.4364×10^{-4}	-3.3285×10^{-2}	-1.1263	-1.2116×10^{1}
$-33.3 > T \geq -36.2$	-1.7424×10^{-4}	-2.1228×10^{-2}	-9.2188×10^{-1}	-1.1881×10^{1}
$F_3(T) = a_3T^3 + b_3T^2 + c_3T + d_3$				
Temperature (°C)	a_3	b_3	c_3	d_3
$-6.4 \geq T \geq -22.8$	-5.5615×10^{-6}	-3.4648×10^{-4}	-9.3360×10^{-3}	-4.6587×10^{-2}
$-22.8 \geq T \geq -33.3$	-4.4404×10^{-4}	-4.3059×10^{-2}	-1.4537	-1.5972×10^{1}
$-33.3 > T \geq -36.2$	-2.2481×10^{-4}	-2.7533×10^{-2}	-1.1977	-1.5854×10^{1}

Table S3. Phase behavior functions for the binary solutions NaCl and $MgSO_4$ derived from a best fit to the output of FREZCHEM v15.1. The piecewise polynomial functions were optimized to ensure that they were continuous across the temperature domain and that $F_1(0) = 0$ and $F_2(0) = \frac{\rho_w(T=T_m)}{\rho_i(T=T_m)} - 1$. Note that because no salts precipitate at temperatures higher than the eutectic temperature, F_3 is zero. Brine is no longer stable below the eutectic temperature (−21.3 °C for NaCl and −3.5 °C for $MgSO_4$).

		$F_1(T) = a_1T^3 + b_1T^2 + c_1T + d_1$			
Species	Temperature (°C)	a_1	b_1	c_1	d_1
NaCl	$0 \geq T \geq -21.3^a$	-7.0940×10^{-4}	-2.4083×10^{-1}	-1.7786×10^{1}	4.4811×10^{-2}
$MgSO_4$	$0 \geq T \geq -3.5^a$	1.8483	1.6781×10^{-1}	-7.8748×10^{1}	1.9840×10^{-1}
		$F_2(T) = a_2T^3 + b_2T^2 + c_2T + d_2$			
Species	Temperature (°C)	a_2	b_2	c_2	d_2
NaCl	$0 \geq T \geq -21.3^a$	-2.8790×10^{-6}	-2.8102×10^{-4}	-1.4350×10^{-2}	9.0709×10^{-2}
$MgSO_4$	$0 \geq T \geq -3.5^a$	1.3459×10^{-3}	-3.8949×10^{-3}	-8.8293×10^{-2}	9.0895×10^{-2}

[a]We note that the eutectic temperatures obtained from FREZCHEM v15.1 differ slightly from those published in the literature. Estimated eutectic temperatures for NaCl range from −21 °C to −22.4 °C (Drebushchak et al., 2019), although recent works adopt a eutectic temperature of -21.1 ± 0.1 °C (Drebushchak et al., 2017; Light et al., 2009; Bode et al., 2015). The eutectic temperature for $MgSO_4$ is estimated to be −3.9 °C (Genceli et al., 2007; Fortes et al., 2008). PHREEQC predicts eutectic temperatures of −21.1 °C for NaCl and −3.8 °C for $MgSO_4$, using the ColdChem database, and eutectic temperatures of −21.1 °C for NaCl and −3.4 °C for $MgSO_4$, using the frezchem database.

Table S4. Phase behavior functions for chloride analog endmember composition for Europa's ocean derived from FREZCHEM v15.1. The temperature breakpoint precedes a major precipitation event that occurs along the freezing pathway (i.e., the formation of hydrohalite at −22.5 °C). F_3 is zero above −6.1 °C (i.e., where mirabilite begins to form) since salt does not precipitate above this temperature. Brine is no longer stable below the eutectic temperature of −32.2 °C. The piecewise polynomial functions were optimized to ensure that they were continuous across their domain and that $F_1(0) = 0$ and $F_2(0) = \frac{\rho_w(T=T_m)}{\rho_i(T=T_m)} - 1$.

$F_1(T) = a_1T^3 + b_1T^2 + c_1T + d_1$				
Temperature (°C)	a_1	b_1	c_1	d_1
$0 \geq T \geq -22.4$	-1.1294×10^{-3}	-2.8149×10^{-1}	-1.9146×10^{1}	0
$-22.4 \geq T \geq -32.2$	-6.0432×10^{-1}	-5.6265×10^{1}	-1.8131×10^{3}	-1.8873×10^{4}
$F_2(T) = a_2T^3 + b_2T^2 + c_2T + d_2$				
Temperature (°C)	a_2	b_2	c_2	d_2
$0 \geq T \geq -22.4$	-3.2037×10^{-6}	-3.1727×10^{-4}	-1.6009×10^{-2}	9.0673×10^{-2}
$-22.4 \geq T \geq -32.2$	-4.8362×10^{-4}	-4.5048×10^{-2}	-1.4516	-1.5023×10^{1}
$F_3(T) = a_3T^3 + b_3T^2 + c_3T + d_3$				
Temperature (°C)	a_3	b_3	c_3	d_3
$-6.1 \geq T \geq -22.4$	-5.5705×10^{-6}	-3.3455×10^{-4}	-8.7581×10^{-3}	-4.1939×10^{-2}
$-22.4 \geq T \geq -32.2$	-6.5682×10^{-4}	-6.1217×10^{-2}	-1.9691	-2.0724×10^{1}

Table S5. Phase behavior functions for sulfate analog endmember composition for Europa's ocean derived from FREZCHEM v15.1. The temperature breakpoint precedes a major precipitation event that occurs along the freezing pathway (i.e., the formation of meridianiite at −5.7 °C). F_3 is zero above −3.4 °C in the SO_4-dominated case (i.e., where mirabilite begins to form) since salt does not precipitate above this temperature. Brine is no longer stable below the eutectic temperature of −32.2 °C. The piecewise polynomial functions were optimized to ensure that they were continuous across their domain and that $F_1(0) = 0$ and $F_2(0) = \frac{\rho_w(T=T_m)}{\rho_i(T=T_m)} - 1$.

$F_1(T) = a_1T^3 + b_1T^2 + c_1T + d_1$				
Temperature (°C)	a_1	b_1	c_1	d_1
$0 \geq T \geq -5.6$	1.8370×10^{-1}	3.3590×10^{-1}	-5.0106×10^{1}	0
$-5.6 \geq T \geq -32.2$	-1.9041×10^{-1}	-1.4282×10^{1}	-4.3325×10^{2}	-1.7529×10^{3}
$F_2(T) = a_2T^3 + b_2T^2 + c_2T + d_2$				
Temperature (°C)	a_2	b_2	c_2	d_2
$0 \geq T \geq -5.6$	2.4977×10^{-5}	-1.4689×10^{-3}	-5.4060×10^{-2}	9.0673×10^{-2}
$-5.6 \geq T \geq -32.2$	-1.9265×10^{-4}	-1.4447×10^{-2}	-4.3544×10^{-1}	-1.6763
$F_3(T) = a_3T^3 + b_3T^2 + c_3T + d_3$				
Temperature (°C)	a_3	b_3	c_3	d_3
$-3.4 \geq T \geq -5.6$	1.2940×10^{-3}	1.5725×10^{-2}	3.8278×10^{-2}	2.1866×10^{-3}
$-5.6 \geq T \geq -32.2$	-3.7263×10^{-4}	-2.7554×10^{-2}	-8.0217×10^{-1}	-3.6398

Table S6. Salt minerals precipitating in FREZCHEM v15.1 simulations of our analog endmember compositions for Europa's ocean. The temperature at which a given salt mineral first begins precipitating (i.e., the highest temperature of occurrence) is provided for different simulated ocean salinities $S_b(T = T_0)$ assuming a pressure of 1 atm. Note that for $S_b \geq 100$ ppt certain salts begin precipitating at higher temperatures, influencing the phase behavior functions shown in Fig. S1 and Fig. S2.

$S_b(T = T_0)$ (ppt)	1	10	20	30	40	50	100	150	200	250
Cl-Dominated	Temperature (°C)									
Mirabilite										
$Na_2SO_4{\cdot}10H_2O$	−6.1	−6.1	−6.1	−6.1	−6.1	−6.1	−5.7	−0.2	≥0.0	≥0.0
Hydrohalite										
$NaCl{\cdot}2H_2O$	−22.5	−22.5	−22.5	−22.5	−22.5	−22.5	−22.5	−22.5	−22.5	−13.8
Meridianiite										
$MgSO_4{\cdot}11H_2O$[a]	−32.3	−32.3	−32.3	−32.3	−32.3	−32.3	−32.3	−32.3	−32.3	−32.3
SO_4-Dominated	Temperature (°C)									
Mirabilite										
$Na_2SO_4{\cdot}10H_2O$	−3.4	−3.4	−3.4	−3.4	−3.4	−3.4	−3.4	−2.0	≥0.0	≥0.0
Meridianiite										
$MgSO_4{\cdot}11H_2O$	−5.7	−5.7	−5.7	−5.7	−5.7	−5.7	−5.7	−5.7	−5.7	≥0.0
Hydrohalite										
$NaCl{\cdot}2H_2O$[a]	−32.3	−32.3	−32.3	−32.3	−32.3	−32.3	−32.3	−32.3	−32.3	−32.3

[a]FREZCHEM predicts this salt will precipitate beyond the final convergent temperature step, so we estimate this temperature as 0.1 °C below the eutectic temperature.

Table S7. Salt precipitation sequences obtained by freezing simulations of our analog end-member compositions for Europa's ocean, using PHREEQC and FREZCHEM. In FREZCHEM we define the eutectic temperature as the final convergent temperature step in the simulation; however in PHREEQC, we define it as the temperature where the final moles in assemblage is no longer increasing. Note that for the PHREEQC simulation of the Cl-Dominated composition, both the ColdChem and frezchem databases predict the dissolution of mirabilite once meridianiite starts to form. Because our FREZCHEM simulation does not converge where meridianiite begins to form, this is not represented in our results.

	Temperature, T (°C)			
	Cl-Dominated			
	FREZCHEM		PHREEQC	
	v13.3	v15.1	ColdChem	frezchem
Mirabilite				
$Na_2SO_4{\cdot}10H_2O$	−6.1	−6.1	−6.3	−6.0
Hydrohalite				
$NaCl{\cdot}2H_2O$	−22.5	−22.5	−22.3	−22.4
Meridianiite				
$MgSO_4{\cdot}11H_2O$	-	−32.3[a]	−31.3	−31.9
$MgCl_2{\cdot}12H_2O$	-	-	*	−34.9
Eutectic Temperature	−32.2	−32.2	−35.3	−35.3
	SO4-Dominated			
	FREZCHEM		PHREEQC	
	v13.3	v15.1	ColdChem	frezchem
Mirabilite				
$Na_2SO_4{\cdot}10H_2O$	−3.4	−3.4	−3.4	−3.3
Meridianiite				
$MgSO_4{\cdot}11H_2O$	−5.7	−5.7	−5.7	−5.6
Hydrohalite				
$NaCl{\cdot}2H_2O$	-	−32.3[a]	*	*
Eutectic Temperature	−32.2	−32.2	−31.2	−31.3

[a] FREZCHEM predicts this salt will precipitate beyond the final convergent temperature step, so we estimate this temperature as 0.1 °C below the eutectic temperature of −32.2 °C.

* Although this salt does not precipitate in the simulation, at the final convergent temperature step the saturation index is near zero, suggesting precipitation is likely imminent.

References

Bode, A. A., Pulles, P. G., Lutz, M., Poulisse, W. J., Jiang, S., Meijer, J. A., ... Vlieg, E. (2015). Sodium chloride dihydrate crystals: morphology, nucleation, growth, and inhibition. *Crystal Growth & Design*, *15*(7), 3166–3174.

Cox, G. F., & Weeks, W. F. (1983). Equations for determining the gas and brine volumes in sea-ice samples. *Journal of Glaciology*, *29*(102), 306–316.

Drebushchak, V., Drebushchak, T., Ogienko, A., & Yunoshev, A. (2019). Crystallization of sodium chloride dihydrate (hydrohalite). *Journal of Crystal Growth*, *517*, 17–23.

Drebushchak, V., Ogienko, A., & Yunoshev, A. (2017). Metastable eutectic melting in the nacl-h2o system. *Thermochimica acta*, *647*, 94–100.

Fortes, A., Wood, I., & Knight, K. (2008). The crystal structure and thermal expansion tensor of mgso4–11d2o (meridianiite) determined by neutron powder diffraction. *Physics and Chemistry of Minerals*, *35*(4), 207–221.

Genceli, F. E., Lutz, M., Spek, A. L., & Witkamp, G.-J. (2007). Crystallization and characterization of a new magnesium sulfate hydrate mgso4· 11h2o. *Crystal Growth and Design*, *7*(12), 2460–2466.

Light, B., Brandt, R. E., & Warren, S. G. (2009). Hydrohalite in cold sea ice: Laboratory observations of single crystals, surface accumulations, and migration rates under a temperature gradient, with application to "snowball earth". *Journal of Geophysical Research: Oceans*, *114*(C7).

Marion, G., Farren, R., & Komrowski, A. (1999). Alternative pathways for seawater freezing. *Cold Regions Science and Technology*, *29*(3), 259–266.

Marion, G., Kargel, J., Catling, D., & Lunine, J. (2012). Modeling ammonia–ammonium

aqueous chemistries in the solar system's icy bodies. *Icarus*, *220*(2), 932–946.

Marion, G., Kargel, J. S., Catling, D. C., & Jakubowski, S. D. (2005). Effects of pressure on aqueous chemical equilibria at subzero temperatures with applications to europa. *Geochimica et Cosmochimica Acta*, *69*(2), 259–274.

Marion, G., Millero, F., & Feistel, R. (2009). Precipitation of solid phase calcium carbonates and their effect on application of seawater s a–t–p models. *Ocean Science*, *5*(3), 285–291.

Petrich, C., & Eicken, H. (2017). Overview of sea ice growth and properties. *Sea ice*, 1–41.

Vancoppenolle, M., Madec, G., Thomas, M., & McDougall, T. J. (2019). Thermodynamics of sea ice phase composition revisited. *Journal of Geophysical Research: Oceans*, *124*(1), 615–634.